# Turbulent transport and mixing in transitional Rayleigh-Taylor unstable flow: A priori assessment of gradient-diffusion and similarity modeling

Oleg Schilling and Nicholas J. Mueschke

# Turbulent transport and mixing in transitional Rayleigh–Taylor unstable flow: *a priori* assessment of gradient-diffusion and similarity modeling

Oleg Schilling*

*Lawrence Livermore National Laboratory, Livermore, California 94550, USA*

Nicholas J. Mueschke[†]

*Department of Mechanical Engineering, Texas A&M University, College Station, Texas 77843, USA*

(Dated: November 13, 2017)

Data from a $1152 \times 760 \times 1280$ direct numerical simulation [Mueschke & Schilling, Phys. Fluids **21**, 014106 (2009)] of a Rayleigh–Taylor mixing layer modeled after a small Atwood number water channel experiment is used to investigate the validity of gradient-diffusion and similarity closures *a priori*. The budgets of the mean flow, turbulent kinetic energy, turbulent kinetic energy dissipation rate, heavy-fluid mass fraction variance, and heavy-fluid mass fraction variance dissipation rate transport equations across the mixing layer were previously analyzed [Schilling & Mueschke, Phys. Fluids **22**, 105102 (2010)] at different evolution times to identify the most important transport and mixing mechanisms. Here, a methodology is introduced to systematically estimate model coefficients as a function of time in the closures of the dynamically significant terms in the transport equations by minimizing the $L_2$-norm of the difference between the model and correlations constructed using the simulation data. It is shown that gradient-diffusion and similarity closures used for the turbulent kinetic energy $K$, turbulent kinetic energy dissipation rate $\epsilon$, heavy-fluid mass fraction variance $S$, and heavy-fluid mass fraction variance dissipation rate $\chi$ equations, capture the shape of the exact, unclosed profiles well over the nonlinear and turbulent evolution regimes. Using order of magnitude estimates [Schilling & Mueschke, Phys. Fluids **22**, 105102 (2010)] for the terms in the exact transport equations and their closure models, it is shown that several of the standard closures for the turbulent production and dissipation (destruction) must be modified to include Reynolds number scalings appropriate for Rayleigh–Taylor flow at small to intermediate Reynolds numbers. The late-time, large Reynolds number coefficients are determined to be different from those used in shear flow applications, and largely adopted in two-equation Reynolds-averaged Navier–Stokes (RANS) models of Rayleigh–Taylor turbulent mixing. In addition, it is shown that the predictions of the Boussinesq model for the Reynolds stress agree better with the data when additional buoyancy-related terms are included. It is shown that an unsteady RANS paradigm is needed to predict the transitional flow dynamics from early evolution times, analogous to the small Reynolds number modifications in RANS models of wall-bounded flows in which the production-to-dissipation ratio is far from equilibrium. Although the present study is specific to one particular flow and one set of initial conditions, the methodology could be applied to calibrations of other Rayleigh–Taylor flows with different initial conditions (which may give different results during the early-time, transitional flow stages, and perhaps asymptotic stage). The implications of these findings for developing high-fidelity eddy viscosity-based turbulent transport and mixing models of Rayleigh–Taylor turbulence are discussed.

PACS numbers: 47.20.-k, 47.20.Ma, 47.27.-i, 47.27.Cn, 47.27.E-, 47.27.ek, 47.27.wj, 47.27.em, 47.27.T-

## I. INTRODUCTION

The modeling of Rayleigh–Taylor turbulent mixing by eddy viscosity turbulence models, such as the two-equation $K$–$\epsilon$ model, requires that the physics embodied in the closures accurately reflect the complex flow dynamics. A previous study[1] used a direct numerical simulation (DNS) data set[2] corresponding to a model of a water channel experiment[3] to investigate the mixing physics and relative importance of terms in the exact mean and turbulent transport equations. The details of

the numerical simulation are discussed in these previous studies. The present study examines *a priori* the applicability of the eddy viscosity hypothesis used in transport models for Rayleigh–Taylor turbulent mixing utilizing this data set. Gradient-diffusion and similarity closures in the turbulent kinetic energy $K$, turbulent kinetic energy dissipation rate $\epsilon$, heavy-fluid mass fraction variance $S$, and heavy-fluid mass fraction variance dissipation rate $\chi$ transport equations are computed directly from the DNS data by defining mean and fluctuating fields using averages in the periodic directions perpendicular to gravity. While the focus of the present investigation is a $K$–$\epsilon$ based model,[4, 5] this study has broader implications for other two-equation models, which also use the same gradient-diffusion and similarity closures but with a different turbulent viscosity constructed using $K$ and an auxiliary turbulent variable (such as a turbulent

length scale $L$). Standard one-point, first-order closures utilize constant model coefficients calibrated so that the models well predict large Reynolds number experimental or simulation data. In applications of such models to small-Reynolds-number flows such as wall-bounded channel flows, modifications are introduced to capture the near-wall viscosity-dominated flow.[6, 7] This is typically achieved in the context of a $K$–$\epsilon$ model[8] by introducing wall functions that effectively interpolate between the near-wall region and the region far from the walls, keeping the functional form of the closures the same.

Rayleigh–Taylor flows differ from shear-driven and wall-bounded flows as they develop from a quiescent state, transitioning to a fully-developed state at sufficiently late times. Thus, the 'quasi-universality' of the closure models assumed for such flows likely precludes their applicability over the early-time linear and weakly-nonlinear stages of Rayleigh–Taylor flow. It is shown here that the variability of the flow physics prior to the turbulent stage can nevertheless be well-captured by such closures, provided that the coefficients are functions of the Reynolds number in unsteady Reynolds-averaged Navier–Stokes (RANS) modeling. It should be emphasized that the transitional behavior of Rayleigh–Taylor flow also depends on the detailed structure of the initial conditions. The present study utilizes data from a specific DNS, and does not investigate the role of variations in the initial conditions on the modeling of this flow.

In the spirit of the DNS study of Chen et al.,[9] the unclosed terms in the turbulence equations are compared here with their respective closure models. The turbulent viscosity coefficient is taken to be its canonical value $C_\mu = 0.09$ and all other model coefficients are determined self-consistently by minimizing the $L_2$ norm between the exact and closed profile of each term across the mixing layer, as a function of time. Correlation and amplitude coefficients are also computed to quantify how well the shape and magnitude of each term is captured by its closure. The turbulence model coefficients approximately asymptote at the largest Reynolds numbers achieved in the simulation, and vary before the onset of turbulence. Using the optimized coefficients determined this way, a three-equation ($K$–$\epsilon$–$S$) or four-equation ($K$–$\epsilon$–$S$–$\chi$) RANS model for transitional, small Atwood number, moderate Reynolds number Rayleigh–Taylor flow is proposed. Here, $S$ denotes the heavy-fluid mass fraction variance (and not a turbulent length scale, for which this symbol is often used) and $\chi$ denotes the heavy-fluid mass fraction variance dissipation rate. These models are not necessarily universal, as the behavior of Rayleigh–Taylor flows is initial conditions-dependent.[10] It is important to note that the present study is specific to one particular flow realization, with one set of initial conditions. Application of the same (or a similar) procedure to other Rayleigh–Taylor flows may give different results (particularly during the early-time, transitional flow stages).

This paper is organized as follows. An overview of RANS models and of gradient-diffusion and similarity

approximations, as well as their limitations vis à vis Rayleigh–Taylor flow, is presented in Sec. II. The terms in the mean and turbulent transport equations are compared at various evolution times with their respective optimized closure models constructed using the DNS data in Sec. III. Correlation and magnitude coefficients are computed for each closure to quantify the agreement between the models and data in the Appendix. Finally, a summary of the principal findings of this *a priori* model study, conclusions, and implications for RANS modeling of transitional Rayleigh–Taylor flow are given in Sec. IV. The models proposed herein will be applied in a companion study to predict turbulent transport and mixing in both small[3] and large Schmidt number[11] Rayleigh–Taylor instability water channel experiments.

## II. OVERVIEW OF REYNOLDS-AVERAGED NAVIER–STOKES TURBULENCE MODELS

### A. Eddy viscosity modeling and the gradient-diffusion and similarity hypotheses

First-order, single-point RANS models require expressions for correlations such as the Reynolds stress tensor $\tau_{ij} = \overline{\rho}\widetilde{u_i'' u_j''}$ and turbulent scalar fluxes $\widetilde{\phi'' u_j''}$ (overbars and tildes denote Reynolds and Favre averages, and single and double primes indicate fluctuations about the Reynolds and Favre averages, respectively). Eddy (or turbulent) viscosity closure formulations utilize the concept that a turbulent flow enhances diffusion of mass, momentum, and energy compared to molecular processes. Boussinesq thus related the Reynolds stress tensor[12]

$$\tau_{ij} \equiv \tau_{ij}^B = \frac{2}{3}\,\overline{\rho}\,K\,\delta_{ij} - 2\,\mu_t\left(\widetilde{S}_{ij} - \frac{\delta_{ij}}{3}\frac{\partial \widetilde{u}_k}{\partial x_k}\right) \quad (1)$$

to the mean strain-rate tensor $\widetilde{S}_{ij} = (1/2)(\partial \widetilde{u}_i/\partial x_j + \partial \widetilde{u}_j/\partial x_i)$, where $K = \widetilde{u_i'' u_i''}/2$ is the turbulent kinetic energy. The turbulent kinetic energy dissipation rate $\epsilon$ is used to construct the turbulent viscosity

$$\nu_t = \frac{\mu_t}{\overline{\rho}} = C_\mu\,\frac{K^2}{\epsilon}\,, \quad (2)$$

where $C_\mu$ is a dimensionless coefficient estimated using experimental or simulation data.[8, 13]

While two-equation models based on a turbulent length scale $L$ are also used,[14] there is no unique definition of $L$, and hence it is unclear which transport equation should be examined. However, the exact turbulent kinetic energy dissipation rate equation can be analyzed using DNS data[1] or potentially using experimental data. Furthermore, as $L$ is typically of the same order as the mixing layer width, it follows that the turbulent length scale describes the large-scale properties of mechanical mixing. By contrast, turbulent dissipation rates

| Coefficient | Term | Shear flow value | Rayleigh–Taylor flow value |
|---|---|---|---|
| $C_\mu$ | turbulent viscosity | 0.0845, 0.09 | 0.09 |
| $\sigma_\rho, \sigma_m$ | turbulent mass flux | 0.50–0.90 | 0.60–1.48 |
| $\sigma_K$ | turbulent flux of $K''$ | 0.72, 1.00 | 0.87–1.00 |
| $\sigma_\epsilon$ | turbulent flux of $\epsilon'$ | 0.72, 1.30 | 1.30 |
| $\sigma_S$ | turbulent flux of $m_1''^2$ | 0.70, 1.00 | – |
| $C_{pu}$ | pressure flux | 0.20 | – |
| $C_{\epsilon 0}$ | buoyancy production of $\epsilon$ | – | 0.815–0.95 |
| $C_{\epsilon 1}$ | shear production of $\epsilon$ | 1.44 | 1.44–1.47 |
| $C_{\epsilon 2}$ | turbulent dissipation of $\epsilon$ | 1.68–1.92 | 1.90–1.92 |
| $C_\chi$ | turbulent dissipation of $S$ | 1.00 | 1.50 |

TABLE I: Coefficients for standard $K$, $\epsilon$, and $S$ transport models[8, 12, 13, 26, 28–31] and as used in Rayleigh–Taylor mixing.[32–34]

describe small-scale properties of scalar mixing, which is the reason why turbulent reacting flow and combustion modeling utilize descriptions based on dissipation rates rather than length scales.[15–17]

Turbulent fluxes in the mean and turbulent transport equations must be modeled. The gradient-diffusion hypothesis states that regions of large values of a mean scalar $\widetilde{\phi}$ diffuse 'down-gradient' and proportional to the intensity of turbulent fluctuations $\widetilde{\phi_\alpha'' u_i''} = -\left(\nu_t/\sigma_\phi\right)\partial\widetilde{\phi}_\alpha/\partial x_i$, where $\sigma_\phi$ is the dimensionless turbulent Schmidt number. Additional closures are required for higher order correlations in the turbulent kinetic energy dissipation rate $\epsilon$, heavy-fluid mass fraction variance $S \equiv \widetilde{m_1''^2}$, and heavy-fluid mass fraction variance dissipation rate $\chi$ transport equations (the 'heavy-fluid' designation will be omitted hereafter), e.g., the buoyancy production and turbulent dissipation in the $\epsilon$ transport equation[1] $P_b^\epsilon = 2\overline{\nu}g_i\overline{(\partial\rho'/\partial x_j)(\partial u_i'/\partial x_j)}$ and $D^\epsilon = 2\overline{\mu}\,\overline{\nu}\overline{(\partial^2 u_i'/\partial x_j \partial x_k)}^2$, respectively. While the gradient-diffusion hypothesis relates turbulent fluxes to mean field gradients, no such hypothesis exists for relating the fluctuating velocity gradient–density gradient correlation in $P_b^\epsilon$ or higher-order correlations in $D^\epsilon$ to mean field gradients. Similarities between the $K$ and $\epsilon$ transport equations are invoked to construct similarity closure hypotheses, in which a proportionality constant relates the closures in the variance and corresponding dissipation rate equations, e.g., $P_b^\epsilon = C_{\epsilon 0}\left(\epsilon/K\right)P_b^K$ (the terms in the $\epsilon$ equation are proportional to those in the $K$ equation and vary on the turbulent time scale $\tau = K/\epsilon$).

### B. Assumptions and limitations of eddy viscosity-based closure models

Several assumptions embodied in eddy viscosity models are incompatible with Rayleigh–Taylor mixing. Thus, models based on extensions of the $K$–$\epsilon$ model[8] are examined here. In the Boussinesq approximation (1), small velocity gradients imply equipartition of the velocity variances $\widetilde{u''^2} \approx \widetilde{v''^2} \approx \widetilde{w''^2} \approx 2K/3$. This is not the case in Rayleigh–Taylor mixing where turbulent trans-

port occurs primarily along the direction aligned with gravity.[1] While Rayleigh–Taylor flows initialized with isotropic perturbations approximately satisfy $\widetilde{u''^2} \approx \widetilde{v''^2}$, the flow considered here and initialized with anisotropic perturbations does not, even at late times.

In the gradient-diffusion hypothesis, turbulent fluxes are assumed to be aligned with their respective mean field gradients, which is often incorrect.[12, 18–23] Modeling Rayleigh–Taylor turbulence is further complicated in that buoyancy is the dominant production mechanism, while mean shear production is negligible.[1] Unless a transport equation is solved for the turbulent mass flux, this term must be modeled algebraically, as in the models evaluated here.

Another limitation of eddy viscosity models is the requirement that the flow be in a state of weak equilibrium, i.e., the production-to-dissipation ratios remain close to unity. The failure of RANS models in flows with large excursions of these ratios from unity is well known.[13, 24] The requirement that $P^K/D^K \approx constant$ is partly due to the large Reynolds number assumption used to formulate similarity closures, where there is a sufficient separation between the production and dissipation scales to allow an inertial energy cascade. Rayleigh–Taylor driven flows are initially quiescent and transition before reaching the Reynolds numbers needed for scale separation. The production-to-dissipation ratios are significantly larger than unity before transition to a three-dimensional, weakly-turbulent state at dimensionless time $t/t_c \approx 17.3$.[1] Thus, the model coefficients vary at small and moderate Reynolds numbers until late-time asymptotic values are approached when the flow achieves a self-similar state.

### III. *A PRIORI* ASSESSMENT AND OPTIMIZATION OF CLOSURE MODELS

Gradient-diffusion and similarity closures of the turbulent fluxes and higher order correlations in the transport equations examined previously[1] are assessed *a priori*[25] to examine the validity of Reynolds-averaged closures for Rayleigh–Taylor turbulent mixing. While
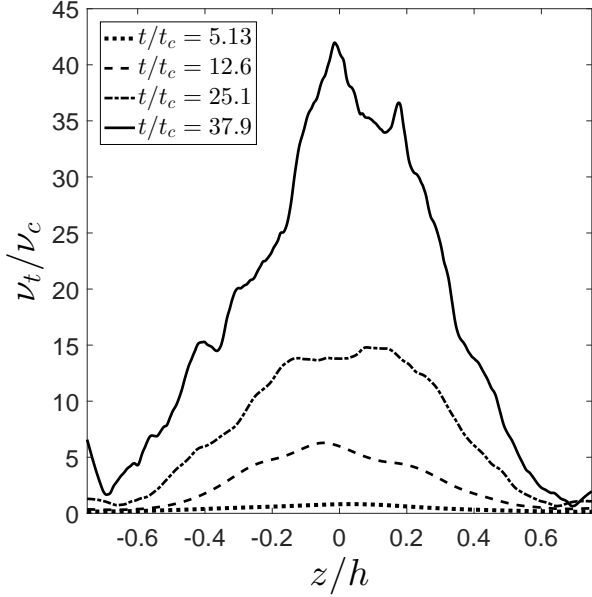
FIG. 1: Profiles of the turbulent viscosity $\nu_t$ (2) normalized by $\nu_c = \ell_c^2/t_c$ at various dimensionless times.

RANS models using constant coefficients calibrated for shear-driven flows have been applied to a variety of steady turbulent flows,[8, 13, 26, 29] there has been much less effort to develop RANS models for unsteady Rayleigh–Taylor mixing.[14, 32–37] For $K$–$\epsilon$ models, most of the previous calibration efforts have focused on the coefficients in the buoyancy production terms. Self-similar solutions were derived for small Atwood number Rayleigh–Taylor flow[32, 33] to estimate the coefficient in the buoyancy production term that best reproduced the growth of a small Atwood number Rayleigh–Taylor mixing layer. A self-similar analysis of the $K$–$L$–$a$ BHR model was performed, and coefficients applicable to either a $\epsilon$- or $L$-based model were estimated (the turbulent length scale was denoted by $S$ in this paper).[37] Thus, the coefficients used in Rayleigh–Taylor mixing are a combination of those used for shear-driven flows and additional coefficients in the buoyancy production terms obtained from an *a posteriori* comparison of model predictions to limited experimental data (e.g., the mixing layer width and its growth rate). Coefficients in typical transport models applied to shear and Rayleigh–Taylor flows are summarized in Table I.

A different approach is used here: terms from the transport equations are compared *a priori* with their respective closures,[9, 38–40] where each modeled term is constructed from Reynolds or Favre mean and fluctuating fields calculated from the DNS, and the optimal coefficients providing best agreement between the exact profiles and their models are determined. In doing so, a measure of the small-Reynolds-number applicability of such models becomes apparent, which is closely related to the open issue of RANS model initialization for Rayleigh–

Taylor flow. For all of the mean and turbulence budgets presented, quantities will be nondimensionalized using density, length, and time scales corresponding to linear instability theory:[1]

$$\rho_c = \frac{\rho_1 + \rho_2}{2} \ , \ \ell_c = \left(\frac{\nu^2}{g\,A}\right)^{1/3} \ , \ t_c = \left(\frac{\nu}{g^2 A^2}\right)^{1/3} \ , \ (3)$$

which are $\rho_c = 0.998$ g/cm$^3$, $\ell_c = 0.051$ cm, and $t_c = 0.264$ s for the flow considered here with $g = 981$ cm/s$^2$ in the $z$-direction, $\nu = 0.01$ cm$^2$/s and $A = 7.5 \times 10^{-4}$. The velocity scale is $u_c = \ell_c/t_c = 0.194$ cm/s. Order of magnitude estimates of the terms in the transport equations in Appendix B of Ref. 1 are used together with similar estimates for the closures to determine any additional Reynolds and Schmidt number scalings.

### A. Determination of optimal model coefficients

*A priori* optimal turbulence model coefficients are determined using a methodology similar to the procedure that provides an estimate of the minimal error that an ideal subgrid-scale model will generate.[41] Consider the exact DNS profile $E(z,t)$ and modeled profile $M(z,t;C_\phi)$ depending on a given model coefficient $C_\phi$. The optimal coefficient is determined by minimizing the $L_2$-norm of the difference between $E(z,t)$ and $M(z,t;C_\phi)$ over the mixing layer $z \in [h_s, h_b]$,

$$L_2(C_\phi, t) = \int_{h_s}^{h_b} \left[E(z,t) - M(z,t;C_\phi)\right]^2 dz \, , \quad (4)$$

where $h_b(t)$ and $h_s(t)$ are the bubble and spike front widths at time $t$. Algebraically solving for $C_\phi$ can produce singularities if $E(z,t)$ or $M(z,t;C_\phi)$ change sign (as in the case of turbulent fluxes). Most profiles extend somewhat beyond the mixing layer boundaries determined by $h_s$ and $h_b$; however, widening the integration limits in Eq. (4) did not change the coefficient values.

Qualitative assessments are performed by comparison of the profiles predicted by the optimized models with the profiles constructed using the DNS data. As the ratio multiplying each closed term is either of the form $C_\mu/\sigma_\phi$ or $C_{Zm}C_\mu/\sigma_\phi$, where $C_{Zm}$ is a coefficient in the transport equation for the generic dissipation rate $Z = (\epsilon, \chi)$, the value of $C_\mu$ is fixed at 0.09and is not optimized.[42] In addition, the predicted self-similar spreading rate of a shear mixing layer depends on this value as well as on $C_{\epsilon 1}$–the coefficient in the closure of the shear production in the turbulent kinetic energy dissipation rate equation. Thus, changing $C_\mu$ would entail changing other coefficients in order to reproduce the experimental growth rate, e.g., Ref. 43. Profiles of the turbulent viscosity $\nu_t$ from the DNS are shown in Fig. 1. Beyond $t/t_c \sim 5.13$, $\nu_t$ exceeds the kinematic viscosity $\overline{\nu} = 0.01$ cm$^2$/s; by the end of the simulation, the peak value $\nu_t/\overline{\nu} \sim 40$ is reached near the center plane $z = 0$. The peak turbulent Reynolds number

reached is $\mathrm{Re}_t = K^2/(\epsilon\,\overline{\nu}) = \nu_t/(C_\mu\overline{\nu}) \sim 400$; all values of $\mathrm{Re}_t$ are evaluated on the center plane.

The predictive capability of a model can be quantified by the correlation coefficient[38]

$$r(C_\phi, t) = \frac{\int_{h_s}^{h_b} \left[E(z,t) - \overline{E}(t)\right]\left[M(z,t;C_\phi) - \overline{M}(C_\phi,t)\right] dz}{\sqrt{\int_{h_s}^{h_b}\left[E(z,t) - \overline{E}(t)\right]^2 dz \int_{h_s}^{h_b}\left[M(z,t;C_\phi) - \overline{M}(C_\phi,t)\right]^2 dz}}, \tag{5}$$

where

$$\overline{E}(t) = \frac{1}{h(t)} \int_{h_s}^{h_b} E(z,t)\,dz\,, \tag{6a}$$

$$\overline{M}(C_\phi, t) = \frac{1}{h(t)} \int_{h_s}^{h_b} M(z,t;C_\phi)\,dz \tag{6b}$$

are the spatial averages of $E(z,t)$ and $M(z,t;C_\phi)$ over the mixing layer. An exact correlation between the model and the DNS data gives $r = 1$, if there is no correlation $r = 0$, and if the model and data are exactly anti-correlated $r = -1$. However, $r(C_\phi,t)$ only determines how well the model is *correlated with* the DNS data, but does not determine how well the model compares in *magnitude* to the DNS data. A ratio of the magnitude of the model profile to the DNS profile is formulated as

$$a(C_\phi, t) = \sqrt{\frac{\int_{h_s}^{h_b} M(z,t;C_\phi)^2\,dz}{\int_{h_s}^{h_b} E(z,t)^2\,dz}}\,, \tag{7}$$

so that the model over-predicts the data if $a > 1$, and the model under-predicts the data if $a < 1$. Thus, $r$ and $a$ provide measures of how well the model is correlated with the data and how close the model is to the data as the flow evolves through the linear, weakly-nonlinear, nonlinear, and transitional stages.

### B. The mean transport equations

The mean flow dynamics are determined by the mean vertical momentum and mass fraction transport equations. The analysis of turbulent transport and mixing processes is discussed in Ref. 1. For the small Atwood number mixing layer considered here, the mean velocity remains very small during the evolution of the Rayleigh–Taylor flow. Thus, the mean advection terms are negligible. For generality and potential applications to larger Atwood number flows, both Reynolds and Favre fluctuating quantities are used: for very small Atwood number, $\widetilde{\phi}_\alpha \approx \overline{\rho\phi}_\alpha/\overline{\rho} \approx \overline{\phi}_\alpha$.

It was shown that the mean vertical momentum equation (6) of Ref. 1 reduces to generalized hydrostatic equilibrium

$$\overline{\rho}\,g \approx -\frac{\partial}{\partial z}(\overline{p} + \tau_{33})\,, \tag{8}$$

where the Reynolds stress is $\tau_{33} = \overline{\rho}\widetilde{w''^2}$. Furthermore, the Reynolds stress contribution $\partial\tau_{33}/\partial z$ is much smaller than the mean pressure gradient contribution, indicating that turbulence has a relatively small influence on the mean momentum evolution. However, the Reynolds stress gradient may not be negligible for larger Atwood number flows. The heavy-fluid mean mass fraction equation (7) of Ref. 1 reduces to

$$\overline{\rho}\,\frac{\partial\widetilde{m}_1}{\partial t} \approx -\frac{\partial}{\partial z}\left(\overline{\rho}\,\widetilde{m_1''\,w''}\right) \tag{9}$$

as the molecular diffusion $(\overline{\mu}/\mathrm{Sc})\,\partial\widetilde{m}_1/\partial x_j$ is negligible compared to the turbulent transport.

### C. The turbulent transport equations

The turbulent kinetic energy transport equation (14) of Ref. 1 reduces to

$$\overline{\rho}\,\frac{\partial K}{\partial t} \approx -\overline{w''}\,\frac{\partial\overline{p}}{\partial z} - \overline{\rho}\,\epsilon - \frac{\partial}{\partial z}\left(\overline{\rho}\,\widetilde{K''\,w''} + \overline{p'\,w''}\right) \tag{10}$$

as the mean shear production $\tau_{ij}\partial\widetilde{u}_i/\partial x_j$, viscous flux $\overline{\sigma_{ij}u_i''}$, and pressure–dilatation $\overline{p'\partial u_k''/\partial x_k}$ are very small. The (incompressible) turbulent kinetic energy dissipation rate transport equation (17) of Ref. 1 reduces to

$$\begin{aligned}
\overline{\rho}\,\frac{\partial\epsilon}{\partial t} \approx\ & -2\,\overline{\nu}\,g\,\overline{\frac{\partial\rho'}{\partial x_j}\frac{\partial w'}{\partial x_j}} - 2\,\overline{\mu}\,\overline{\frac{\partial u_i'}{\partial x_k}\frac{\partial u_i'}{\partial x_j}\frac{\partial u_k'}{\partial x_j}} \\
& -2\,\overline{\mu}\,\overline{\nu}\,\overline{\left(\frac{\partial^2 u_i'}{\partial x_j\partial x_k}\right)^2} - \frac{\partial}{\partial z}\left(\overline{\rho\,\epsilon'\,w'} + 2\,\overline{\nu}\,\overline{\frac{\partial p'}{\partial x_k}\frac{\partial w'}{\partial x_k}}\right)
\end{aligned} \tag{11}$$

as the mean shear production proportional to $\partial\overline{u}_i/\partial x_j$, curvature production proportional to $\partial^2\overline{u}_i/\partial x_j\partial x_k$, and molecular dissipation flux $\overline{\mu}\partial\epsilon/\partial x_j$ are small. The mass fraction variance transport equation (19) of Ref. 1 reduces to

$$\begin{aligned}
\overline{\rho}\,\frac{\partial S}{\partial t} \approx\ & -2\,\overline{\rho}\,\widetilde{m_1''\,w''}\,\frac{\partial\widetilde{m}_1}{\partial z} - 2\,\overline{\rho}\chi \\
& -\frac{\partial}{\partial z}\left(\overline{\rho}\,\widetilde{m_1''^2\,w''}\right)
\end{aligned} \tag{12}$$

as the molecular diffusion flux $\overline{\rho}\overline{D}\partial S/\partial x_j$ is small. Finally, the mass fraction variance dissipation rate trans-
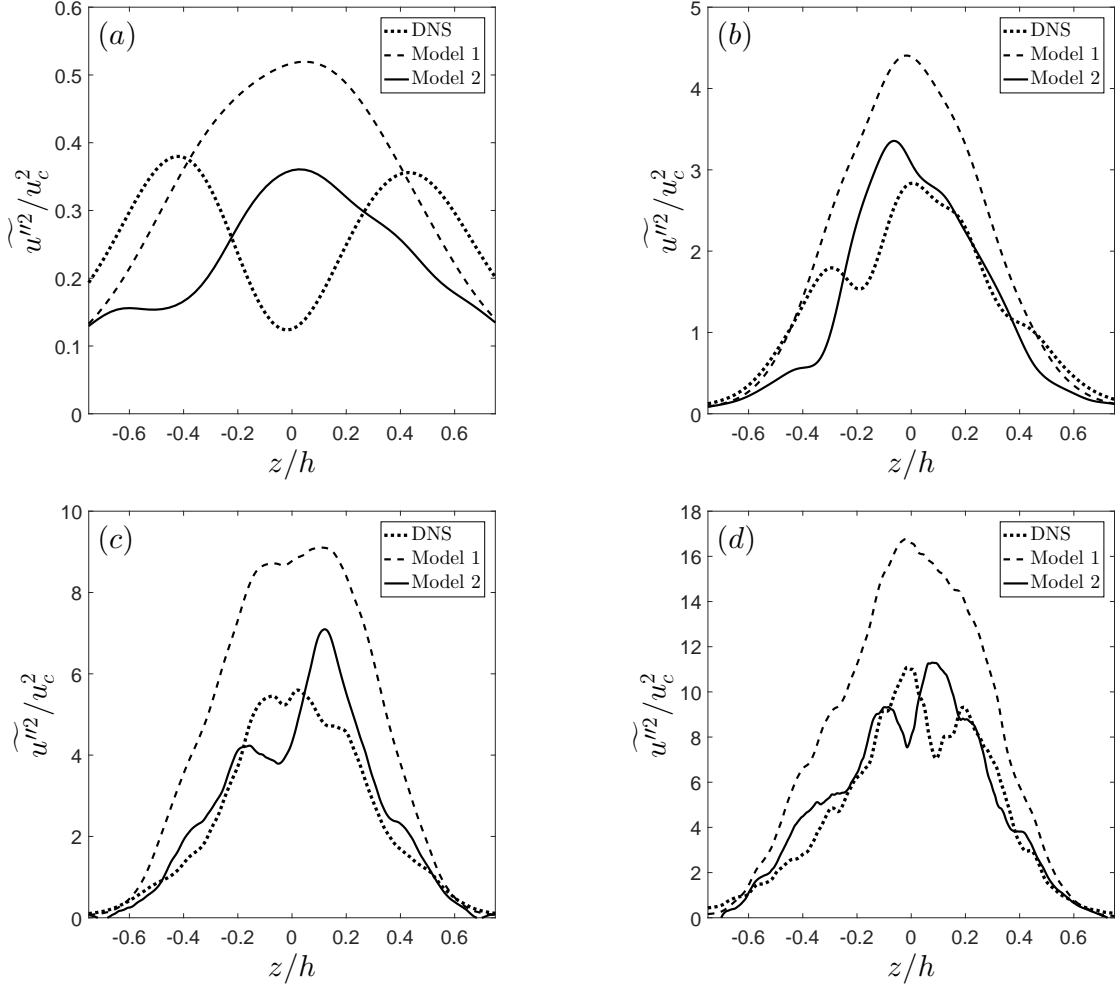
FIG. 2: Profiles of the velocity variance $\widetilde{u''^2}$ normalized by $u_c^2$ and its Boussinesq and generalized Boussinesq gradient-diffusion closures (1) (Model 1) and (15) (Model 2) at (a) $t/t_c = 5.13$, (b) 12.6, (c) 25.1, and (d) 37.9.

port equation (22) of Ref. 1 reduces to

$$\overline{\rho}\,\frac{\partial \chi}{\partial t} \approx -2\overline{D}\,\overline{\rho\,\frac{\partial m_1''}{\partial x_i}\,\frac{\partial m_1''}{\partial x_j}\,\frac{\partial u_j''}{\partial x_i}} \qquad (13)$$
$$-2\overline{D}^2\,\overline{\rho\left(\frac{\partial^2 m_1''}{\partial x_i \partial x_j}\right)^2} - \frac{\partial}{\partial z}\left(\overline{\rho}\,\widetilde{\chi'' w''}\right)$$

as the terms proportional to the mean fields gradients $\partial \widetilde{m}_1/\partial x_j$, $\partial \widetilde{u}_j/\partial x_i$, and $\partial^2 \widetilde{m}_1/\partial x_i \partial x_j$, and molecular diffusion flux $\overline{\rho}\overline{D}\partial \chi/\partial x_j$ are small. Note that in the *a priori* analysis of turbulent transport performed here, there is no loss of generality as a result of neglecting the mean advection terms because they do not require closure.

### D. Generalized Boussinesq Reynolds stress model

In shear-driven turbulent flows, accurate prediction of the Reynolds stresses is crucial for modeling the mean shear velocity. While the Boussinesq closure for $\tau_{ij}$ is

sufficiently accurate for many flows,[6] it is generally inappropriate for Rayleigh–Taylor mixing due to the sustained anisotropy of velocity fluctuations. While the Boussinesq model predicts the shapes of $\widetilde{u_i''^2}$, it does not predict their magnitudes. While the mean momentum equation and shear production rates of $K$ and $\epsilon$ require a model for $\tau_{ij}$, it was shown that the shear productions $P_s^K$ and $P_s^\epsilon$ are negligible compared to the buoyancy productions $P_b^K$ and $P_b^\epsilon$, and the gradient of the Reynolds stress is small compared to the mean pressure gradient for the present flow.[1] Nevertheless, a *complete* RANS model for Rayleigh–Taylor turbulence should include a sufficiently accurate model for $\tau_{ij}$, irrespective of the Atwood number.

Using the traceless, symmetric baroclinic tensor[45]

$$\overline{A}_{ij} = \frac{\partial \overline{\rho}}{\partial x_i}\,\frac{\partial \overline{p}}{\partial x_j} + \frac{\partial \overline{\rho}}{\partial x_j}\,\frac{\partial \overline{p}}{\partial x_i} - \frac{2}{3}\,\delta_{ij}\,\frac{\partial \overline{\rho}}{\partial x_k}\,\frac{\partial \overline{p}}{\partial x_k}, \qquad (14)$$
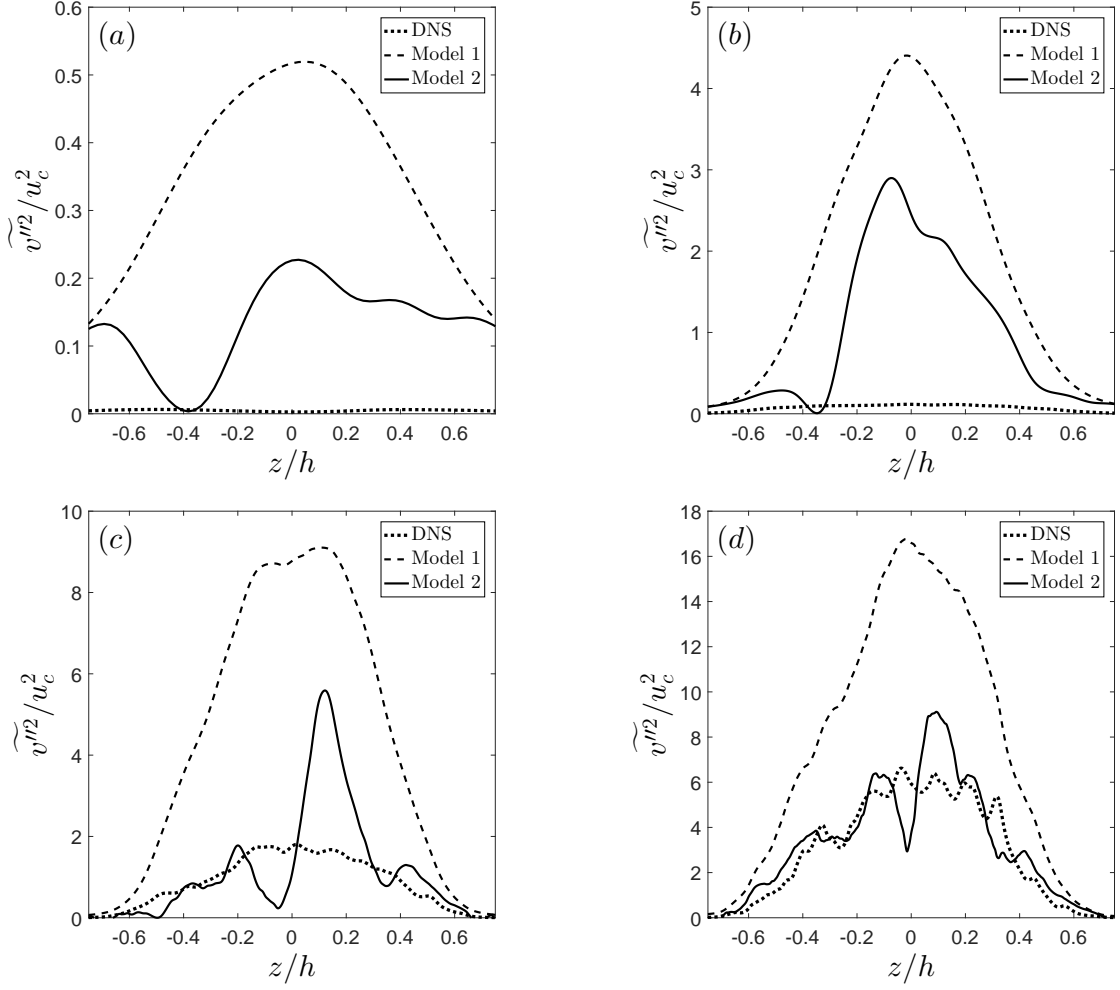
FIG. 3: Profiles of the velocity variance $\widetilde{v''^2}$ normalized by $u_c^2$ and its Boussinesq and generalized Boussinesq gradient-diffusion closures (1) (Model 1) and (15) (Model 2) at (a) $t/t_c = 5.13$, (b) 12.6, (c) 25.1, and (d) 37.9.

a new model can be proposed as an extension of (1) as

$$\tau_{ij} = \tau_{ij}^B - C_A^{ijkl} \, \nu_t \, \frac{K}{\overline{\rho} \, \epsilon} \, \overline{A}_{kl} \,, \qquad (15)$$

where the $C_A^{ijkl} = C_A^{jikl}$ are dimensionless tensor coefficients, and it is assumed here that $C_A^{ijkl} = C^{(ijkl)} \delta_{ik} \delta_{jl}$. Thus,

$$\tau_{11} \longrightarrow \frac{2}{3} \left( \overline{\rho} \, K + \mu_t \, \frac{\partial \widetilde{w}}{\partial z} \right) \qquad (16)$$
$$+ \frac{2}{3} C_A^{(1111)} \, \nu_t \, \frac{K}{\overline{\rho} \, \epsilon} \, \frac{\partial \overline{\rho}}{\partial z} \, \frac{\partial \overline{p}}{\partial z} \,,$$

$$\tau_{22} \longrightarrow \frac{2}{3} \left( \overline{\rho} \, K + \mu_t \, \frac{\partial \widetilde{w}}{\partial z} \right) \qquad (17)$$
$$+ \frac{2}{3} C_A^{(2222)} \, \nu_t \, \frac{K}{\overline{\rho} \, \epsilon} \, \frac{\partial \overline{\rho}}{\partial z} \, \frac{\partial \overline{p}}{\partial z} \,,$$

$$\tau_{33} \longrightarrow \frac{2}{3} \left( \overline{\rho} \, K - 2 \, \mu_t \, \frac{\partial \widetilde{w}}{\partial z} \right) \qquad (18)$$
$$- \frac{4}{3} C_A^{(3333)} \, \nu_t \, \frac{K}{\overline{\rho} \, \epsilon} \, \frac{\partial \overline{\rho}}{\partial z} \, \frac{\partial \overline{p}}{\partial z} \,,$$

$$\tau_{12} = \tau_{21} = 0 \,, \qquad (19)$$

$$\tau_{13} = \tau_{31} \longrightarrow -\mu_t \, \frac{\partial \widetilde{u}}{\partial z} \,, \quad \tau_{23} = \tau_{32} \longrightarrow -\mu_t \, \frac{\partial \widetilde{v}}{\partial z} \,, \quad (20)$$

where $C_A^{(1111)} \approx C_A^{(2222)} \neq C_A^{(3333)}$ is expected if the flow becomes nearly isotropic in the plane perpendicular to gravity. This model generalizes the dependence of $\tau_{ij}$ on the mean velocity gradient to include the mean density and pressure gradients, and reduces to the Boussinesq model in the constant density limit. From Fig. 1 of Ref. 1, $\partial \overline{\rho}/\partial z > 0$ and $\partial \overline{p}/\partial z < 0$, so that $A_{11}, A_{22} > 0$ and $A_{33} < 0$.
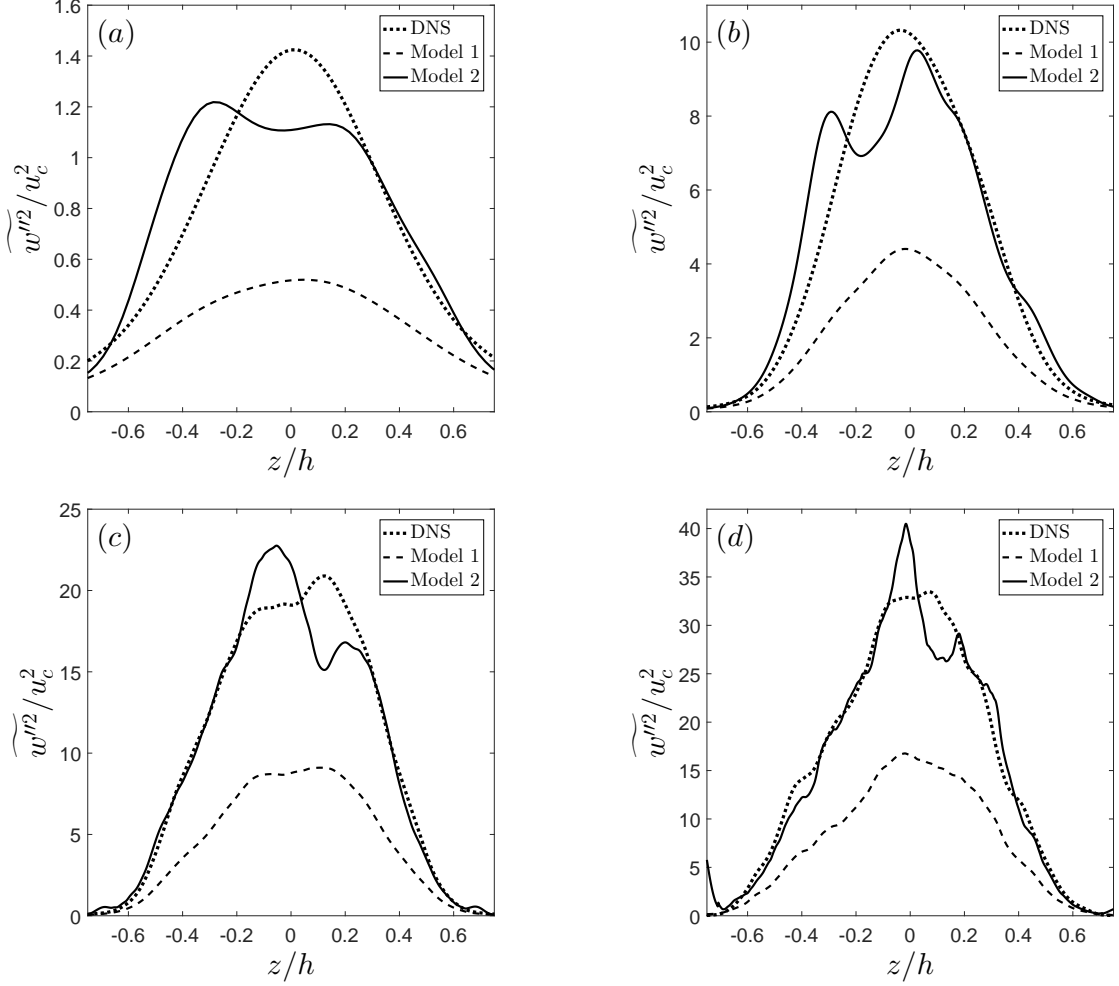
FIG. 4: Profiles of the velocity variance $\widetilde{w''^2}$ normalized by $u_c^2$ and its Boussinesq and generalized Boussinesq gradient-diffusion closures (1) (Model 1) and (15) (Model 2) at (a) $t/t_c = 5.13$, (b) 12.6, (c) 25.1, and (d) 37.9.

The model (15) is inspired by the algebraic Reynolds stress model ($\beta = 1/T_0$)

$$\overline{v_i' v_j'} = \frac{2}{3} K \delta_{ij} - 2\nu_t \overline{S}_{ij} \tag{21}$$
$$+ C_T \beta \frac{K}{\epsilon} \left( g_i \overline{T' u_j'} + g_j \overline{T' u_i'} - \frac{2}{3} \delta_{ij} g_k \overline{T' u_k'} \right)$$

previously used in transient-RANS and very large-eddy simulation of incompressible turbulent convection.[46–48] Here, density fluctuations are analogous to temperature fluctuations. Thus, taking $g_i \to (1/\overline{\rho}) \partial \overline{p}/\partial x_i$ and $\beta \overline{T' u_i'} \to \overline{\rho' u_i'}/\overline{\rho} = -(\nu_t/\sigma_\rho) \partial \ln \overline{\rho}/\partial x_i$ gives (15).

Requiring the orders of magnitude to agree for the exact Reynolds stress and its closure

$$\tau_{zz} \sim \frac{2}{3} f \overline{\rho} K - 2f \mu_t \left( \widetilde{S}_{zz} - \frac{1}{3} \frac{\partial \widetilde{u}_k}{\partial x_k} \right) - e \frac{K^3}{\overline{\rho} \, \epsilon^2} \overline{A}_{zz}$$
$$\sim \rho_0 \left( f u_h^2 - f u_h \widetilde{v} + egh \right),$$

so that $f = 1$ and $e = u_h^2/(gh) = Fr_h^2$ is the Froude number squared. At large Reynolds numbers, using the self-

similar growth of the mixing layer width, $h(t) = \alpha A g t^2$, $u_h \sim \mathrm{d}h/\mathrm{d}t \sim 2\alpha A g t$. Thus, $u_h^2 \sim 4\alpha A g h$, and therefore $Fr_h \sim 2\sqrt{\alpha A}$. Figures 2–4 show a comparison between the Boussinesq model (1) and the new model (15) for the diagonal components of $\widetilde{u_i'' u_j''}$ from the DNS. As expected for Rayleigh–Taylor flow in which the mean strain-rate is small, the Boussinesq model substantially overpredicts $\widetilde{u''^2}$ and $\widetilde{v''^2}$, and underpredicts $\widetilde{w''^2}$. By contrast, the new model very well matches the DNS at all times. The optimal coefficients $C_A^{(iiii)}$ shown in Fig. 5 begin to slowly decrease following an initial transient. Table III gives the values of $C_A^{(iiii)}$ at various times. Note that beyond $t/t_c \approx 35$ the limited resolution at late times in calculating gradients (as also seen in the oscillations in the model profiles) would overestimate the values of these coefficients.
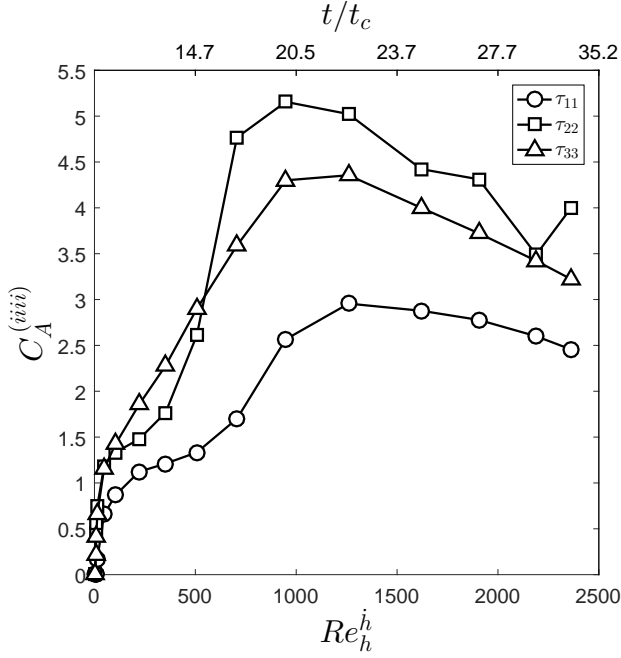
FIG. 5: Evolution of optimal coefficients $C_A^{(iiii)}$ corresponding to the three diagonal Reynolds stress components $\tau_{ii}$.

## E. Gradient-diffusion closures

### 1. Buoyancy production of turbulent kinetic energy

The buoyancy production terms in the turbulent kinetic energy and turbulent kinetic energy dissipation rate equations, $P_b^K$ and $P_b^\epsilon$, are the principal Rayleigh–Taylor instability driving terms. The gradient-diffusion model of the buoyancy production $P_b^K$ in the turbulent kinetic energy equation is given in terms of the density–velocity correlation model[12, 49, 50]

$$\overline{u_j''} = -\frac{\overline{\rho' u_j'}}{\overline{\rho}} = \frac{\nu_t}{\sigma_\rho \overline{\rho}} \frac{\partial \overline{\rho}}{\partial x_j} \qquad (22)$$

or

$$\overline{w''} \longrightarrow \frac{\nu_t}{\sigma_\rho \overline{\rho}} \frac{\partial \overline{\rho}}{\partial z}, \qquad (23)$$

so that

$$\begin{aligned} P_b^K &= -\overline{u_j''} \frac{\partial \overline{p}}{\partial x_j} = -\frac{\nu_t}{\sigma_\rho \overline{\rho}} \frac{\partial \overline{\rho}}{\partial x_j} \frac{\partial \overline{p}}{\partial x_j} \qquad (24) \\ &\longrightarrow -\frac{\nu_t}{\sigma_\rho \overline{\rho}} \frac{\partial \overline{\rho}}{\partial z} \frac{\partial \overline{p}}{\partial z}, \end{aligned}$$

where $\sigma_\rho$ is a dimensionless turbulent Schmidt number. Requiring the orders of magnitude to agree for the exact buoyancy production and its closure

$$P_b^K \sim -f \frac{\nu_t}{\overline{\rho}} \frac{\partial \overline{\rho}}{\partial z} \frac{\partial \overline{p}}{\partial z} \sim f \Delta \rho \, g \, u_h$$

gives $f = \rho_{rms}/\Delta\rho$, so that no additional scalings are expected in (24) (n.b., $\rho_{rms} \propto m_{rms}$ changes slowly at late times[1]). The gradient-diffusion closure of the averaged Favre fluctuating velocity (23) is shown in Fig. 6, where on average both the closure and DNS data agree (with higher amplitude oscillations as time progresses). On average, the DNS profiles are more symmetric than the model profiles about the center plane. The closure (22) has also been used for shock-driven flows[52]; a generalization of this expression to include the mean pressure gradient (appropriate for shocked flows) was used to model a broad set of reshocked Richtmyer–Meshkov instability experiments.[53, 54]

### 2. Turbulent fluxes

The turbulent fluxes have important dynamical effects in Rayleigh–Taylor flow, e.g., the turbulent mass flux controls both the spreading rate of the mixing layer in the mean mass fraction transport and production rates of turbulent kinetic energy and mass fraction variance. Gradient-diffusion models for the turbulent fluxes are of the form $\overline{\rho}\widetilde{\phi_\alpha'' w''} = -\left(\mu_t/\sigma_\phi\right)\partial\widetilde{\phi}_\alpha/\partial z$ and specifically

$$\overline{\rho}\,\widetilde{m_1'' w''} = -\frac{\mu_t}{\sigma_m} \frac{\partial \widetilde{m}_1}{\partial z}, \quad \overline{\rho}\,\widetilde{K'' w''} = -\frac{\mu_t}{\sigma_K} \frac{\partial K}{\partial z}, \qquad (25)$$

$$\overline{\rho}\,\overline{\epsilon' w'} = -\frac{\mu_t}{\sigma_\epsilon} \frac{\partial \epsilon}{\partial z}, \quad \overline{\rho}\,\widetilde{m_1''^2 w''} = -\frac{\mu_t}{\sigma_S} \frac{\partial S}{\partial z}, \qquad (26)$$

$$\overline{\rho}\,\widetilde{\chi'' w''} = -\frac{\mu_t}{\sigma_\chi} \frac{\partial \chi}{\partial z}, \qquad (27)$$

where $\sigma_m, \sigma_K, \sigma_\epsilon, \sigma_S$, and $\sigma_\chi$ are dimensionless turbulent Schmidt numbers. Consider the turbulent kinetic energy flux: requiring the orders of magnitude to agree for the exact flux and its closure

$$F_t^K \sim -f \mu_t \frac{\partial K}{\partial z} \sim f \rho_0 \, u_h^3$$

gives $f = 1$. More generally, a generic turbulent flux corresponding to $\phi_\alpha'' = \left(m_1'', K'', \epsilon', m_1''^2, \chi''\right)$ is $\overline{\rho\phi_\alpha'' w''}$ which is $\mathcal{O}(\rho_0\phi_{\alpha,rms}u_h)$; its closure is

$$F_t^{\widetilde{\phi_\alpha''}} \sim -f \mu_t \frac{\partial \widetilde{\phi_\alpha''}}{\partial z} \sim f \rho_0 \, u_h \, \phi_{\alpha,rms},$$

so that $f = 1$ and no additional scalings are expected.

Comparisons of the gradient-diffusion models with the exact fluxes are shown in Figs. 7–11. Each flux is shown using the optimal turbulent Schmidt number at each time $\sigma_\phi(\mathrm{Re}_h)$ calculated by minimizing the $L_2$-norm difference between the DNS and model profiles. The closures for the mass fraction flux, mass fraction variance flux, and mass fraction variance dissipation rate flux are analogous to those used in turbulent nonpremixed combustion for the
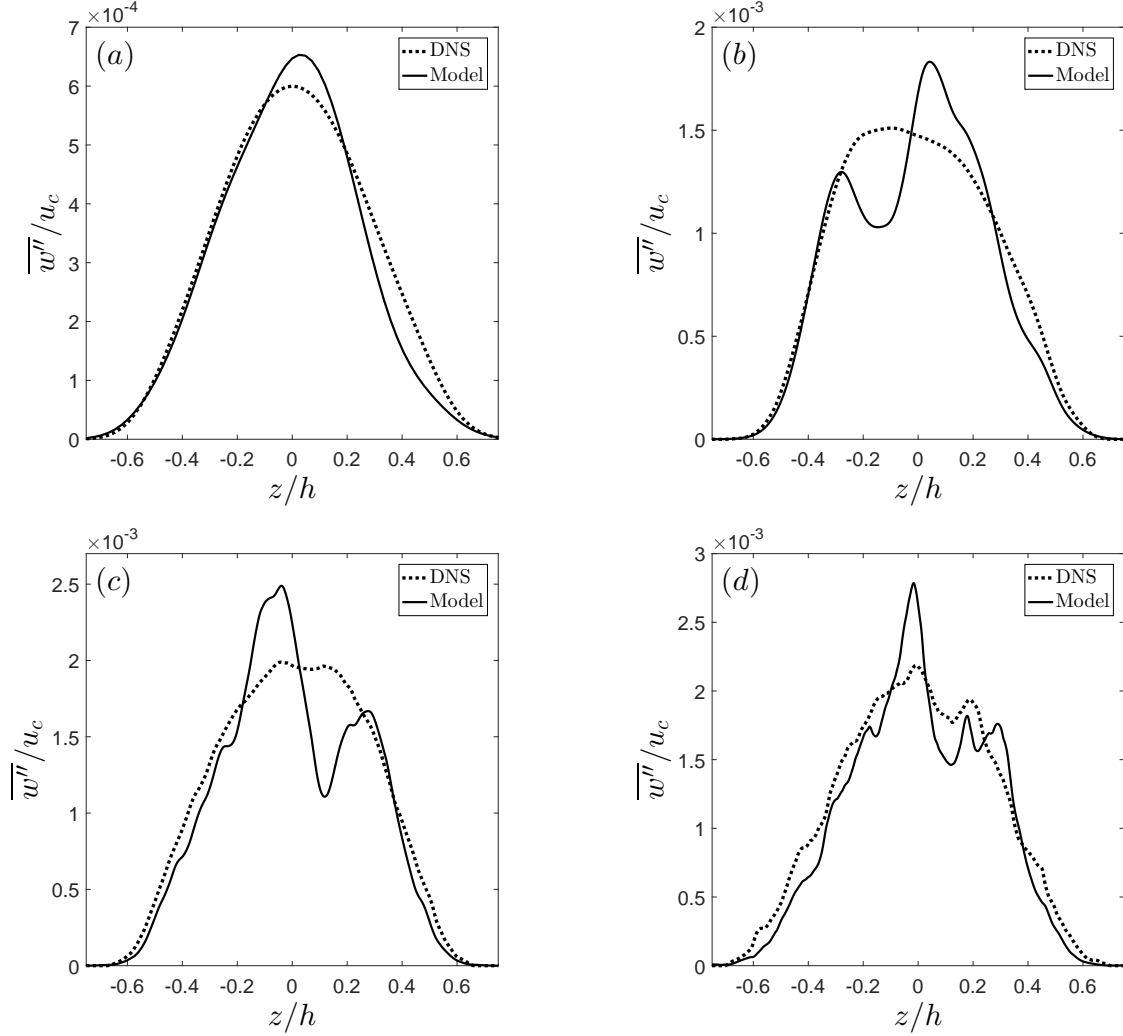
FIG. 6: Profiles of the averaged vertical Favre fluctuating velocity $\overline{w''}$ normalized by $u_c$ and its gradient-diffusion closure (23) at (a) $t/t_c = 5.13$, (b) 12.6, (c) 25.1, and (d) 37.9.

mixture fraction, mixture fraction variance, and mixture fraction variance dissipation rate fluxes.[55] Figures 8–11 (particularly at the latest two times) indicate that the model and DNS do not predict the maxima and minima of the fluxes at the same spatial locations within the mixing layer, although the values of the maxima and minima are in reasonable agreement on average.

The turbulent Schmidt numbers corresponding to each flux shown in Fig. 12 exhibit some expected variability at early times ($t/t_c < 17.3$ or $\mathrm{Re}_h < 500$) as the mixing evolves through the linear and transitional regimes. Most decrease early in time and then grow after transition. However, $\sigma_\epsilon$ and $\sigma_\chi$ both increase at early times, reach maximum values at $t/t_c \approx 12.6$, and then rapidly decrease. Once the mixing layer evolves beyond the transitional regime ($\mathrm{Re}_h \gtrsim 500$), the turbulent Schmidt numbers relax to

$$\sigma_\rho \approx 0.08 \,, \ \sigma_K \approx 0.09 \,, \ \sigma_\epsilon \approx 0.10 \,, \qquad (28)$$

$$\sigma_m \approx 0.08 \,, \ \sigma_S \approx 0.07 \,, \ \sigma_\chi \approx 0.15 \,. \qquad (29)$$

The turbulent Schmidt numbers for the scalar fields exhibit a greater dynamic range and are more sensitive to $\mathrm{Re}_h$. Table III gives the values of $\sigma_\rho$, $\sigma_K$, $\sigma_\epsilon$, $\sigma_m$, $\sigma_S$, and $\sigma_\chi$ at various times. Beyond $t/t_c \approx 32.5$ the limited resolution at late times in calculating gradients due to the decreasing number of turbulent structures over which averages are computed (as also seen in the oscillations in the mean field gradients and model profiles) would slightly overestimate these coefficients.

The turbulent Schmidt numbers are much smaller than used in shear-driven flows. Applications of two-equation $K$–$\epsilon$ models to Rayleigh–Taylor mixing have used larger turbulent Schmidt numbers (see Table I). These studies have either cited other buoyancy-driven applications[33] or used an *a posteriori* determination of each turbulent Schmidt number.[34, 35] The present work is the first to directly and systematically calculate the turbulent Schmidt numbers for a four-equation $K$–$\epsilon$–$S$–$\chi$ model
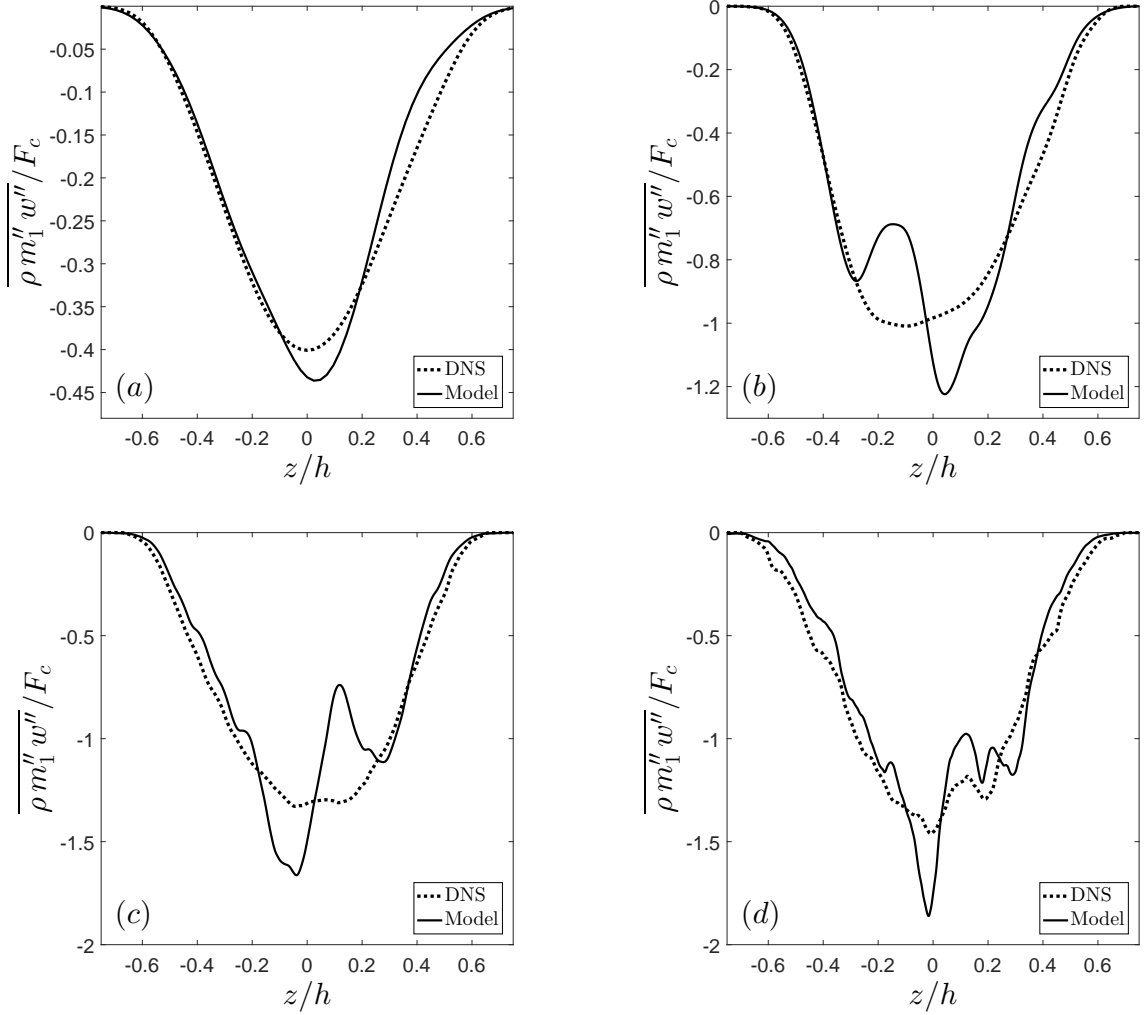
FIG. 7: Profiles of the vertical turbulent heavy-fluid mass fraction flux $\widetilde{\overline{\rho m_1'' w''}}$ normalized by $F_c = \rho_c u_c$ and its gradient-diffusion closure (25) at (a) $t/t_c = 5.13$, (b) 12.6, (c) 25.1, and (d) 37.9.

and illustrate the dynamic behavior of the coefficients in transitional Rayleigh–Taylor turbulent flow.

### 3. Pressure fluxes

The pressure flux $\overline{p' w''}$ is non-negligible, has a complex shape, and bifurcates in its transport behavior at an early time in the mixing layer evolution.[1] Most formulations either neglect the pressure flux[27] or combine it with the turbulent kinetic energy flux $\widetilde{K'' u_i''}$.[28] In the model investigated here, the pressure flux is subtracted from the overall flux of $K$,

$$\overline{p' u_i''} = -C_{pu} \, \overline{\rho} \, \widetilde{K'' u_i''} \tag{30}$$

or

$$\overline{p' w''} = -C_{pu} \, \overline{\rho} \, \widetilde{K'' w''}, \tag{31}$$

with a suggested value $C_{pu} = 0.4$ in homogeneous turbulence.[28] Requiring the orders of magnitude to agree for the exact pressure flux and its closure

$$F_p^K \sim -\overline{\rho} \, \widetilde{K'' w''} \sim f \, \mu_t \, \frac{\partial K}{\partial z} \sim f \, \rho_0 \, u_h^3$$

gives $f = \rho_{rms}/\rho_0$, so that the pressure flux decreases as the root-mean-square density fluctuations decrease.

Profiles of the exact and closed vertical pressure flux are shown in Fig. 13. At very small Reynolds numbers ($\mathrm{Re}_h < 100$), Eq. (31) does not correctly predict the direction of the flux of $K$; this may be rectified by a negative value of $C_{pu}$, as shown in the profile at $t/t_c = 5.13$. For small to moderate Reynolds numbers ($100 < \mathrm{Re}_h < 1500$), the model correctly predicts the flux direction within the mixing layer core $|z/h| \lesssim 0.5$. However, this model does not predict the shape of the profile well, nor does it capture the change in sign of the flux at the boundaries of the layer ($|z/h| \gtrsim 0.5$): this
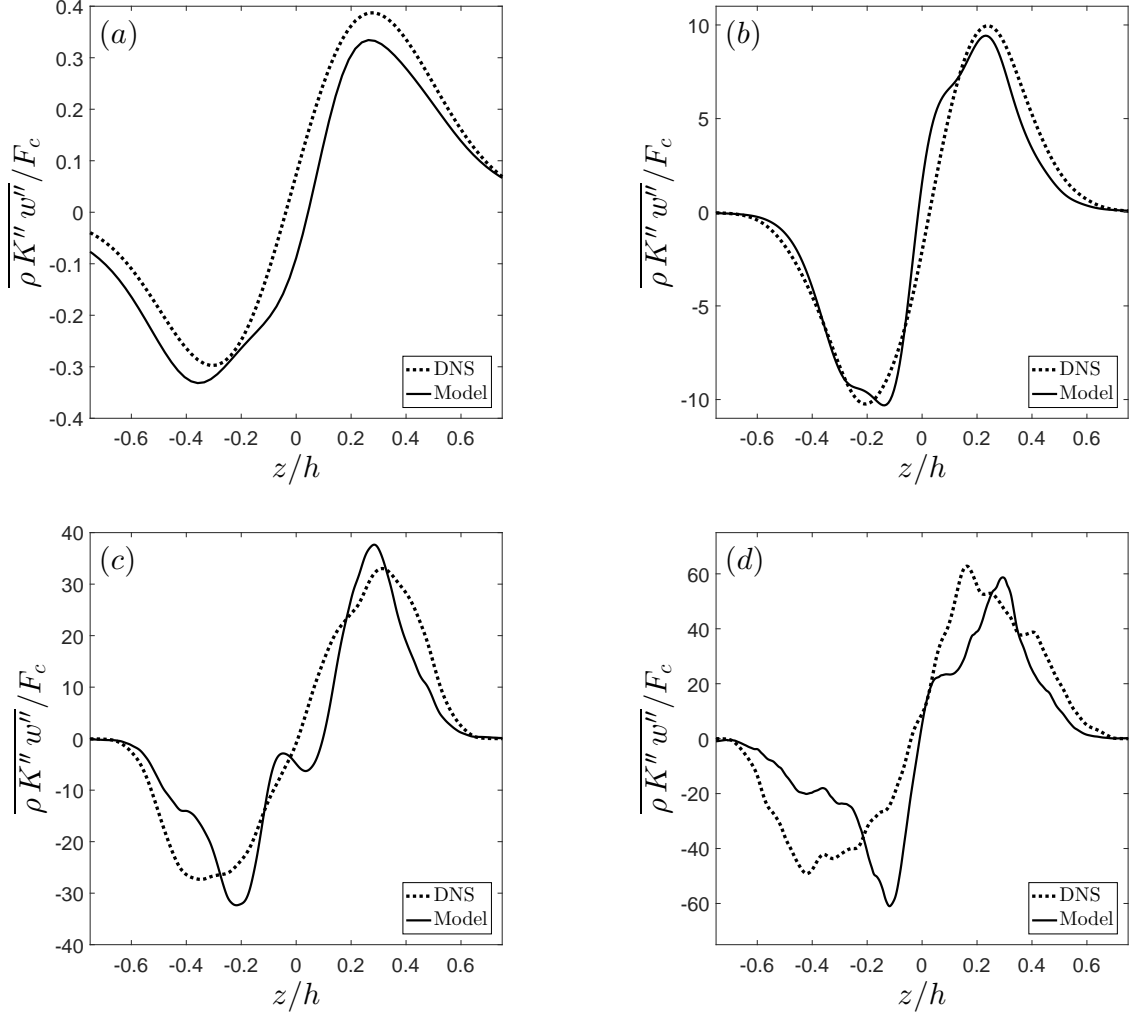
FIG. 8: Profiles of the vertical turbulent kinetic energy flux $\overline{\rho \widetilde{K'' w''}}$ normalized by $F_c = \rho_c u_c^3$ and its gradient-diffusion closure (25) at (a) $t/t_c = 5.13$, (b) 12.6, (c) 25.1, and (d) 37.9.

has significant effects at the mixing layer boundaries and must be captured by any realistic closure.

Similar to the pressure flux of $K$, $\epsilon$ is also transported via pressure fluctuations. While the pressure flux of $K$ has received little attention, much less consideration has been given to the pressure flux of $\epsilon$: neither has been previously examined for Rayleigh–Taylor flow. Using a closure analogous to Eq. (31), consider the new model

$$F_p^\epsilon = 2\,\overline{\nu}\, \overline{\frac{\partial p'}{\partial x_j} \frac{\partial u_i'}{\partial x_j}} = -C_{pu}^\epsilon\, \overline{\rho}\, \overline{\epsilon'\, w'}. \qquad (32)$$

Requiring the orders of magnitude to agree for the exact turbulent kinetic energy dissipation rate pressure flux and its closure

$$F_p^\epsilon \sim -\overline{\rho}\, \overline{\epsilon'\, w'} \sim f\, \mu_t\, \frac{\partial \epsilon}{\partial z} \sim f\, \frac{\mu\, u_h^3}{\lambda^2}$$

gives $f = 1$. The exact and closed $\epsilon$ pressure flux profiles are shown in Fig. 14. Similar to $\overline{p' w''}$, the pressure

flux of $\epsilon$ enhances the vertical turbulent flux $\overline{\rho \epsilon' w'}$ at early times and then transitions to a profile that opposes $\overline{\rho \epsilon' w'}$. Also, the pressure flux of $\epsilon$ exhibits the same complex behavior as $\overline{p' w''}$, where $\epsilon$ is transported away from the mixing layer core at the boundaries of the layer. However, this effect is much smaller than the transport of $K$ away from the mixing layer by pressure fluctuations. This is expected as velocity fluctuations induced in the fluid around the mixing layer remains essentially irrotational, and hence, the dissipation rate of these fluctuations is nearly negligible.

Figure 15 shows the evolution of the optimal coefficients $C_{pu}$ and $C_{pu}^\epsilon$ for the models (31) and (32). As the pressure flux is non-negligible, even beyond the boundaries of the mixing layer, the $L_2$-norm minimization was modified such that the integration limits were changed from $[h_s, h_b]$ to $[-L_z/2, L_z/2]$. Both coefficients are negative before $t/t_c \approx 10$, when the mixing is entering a nonlinear transitional regime. Negative values indicate
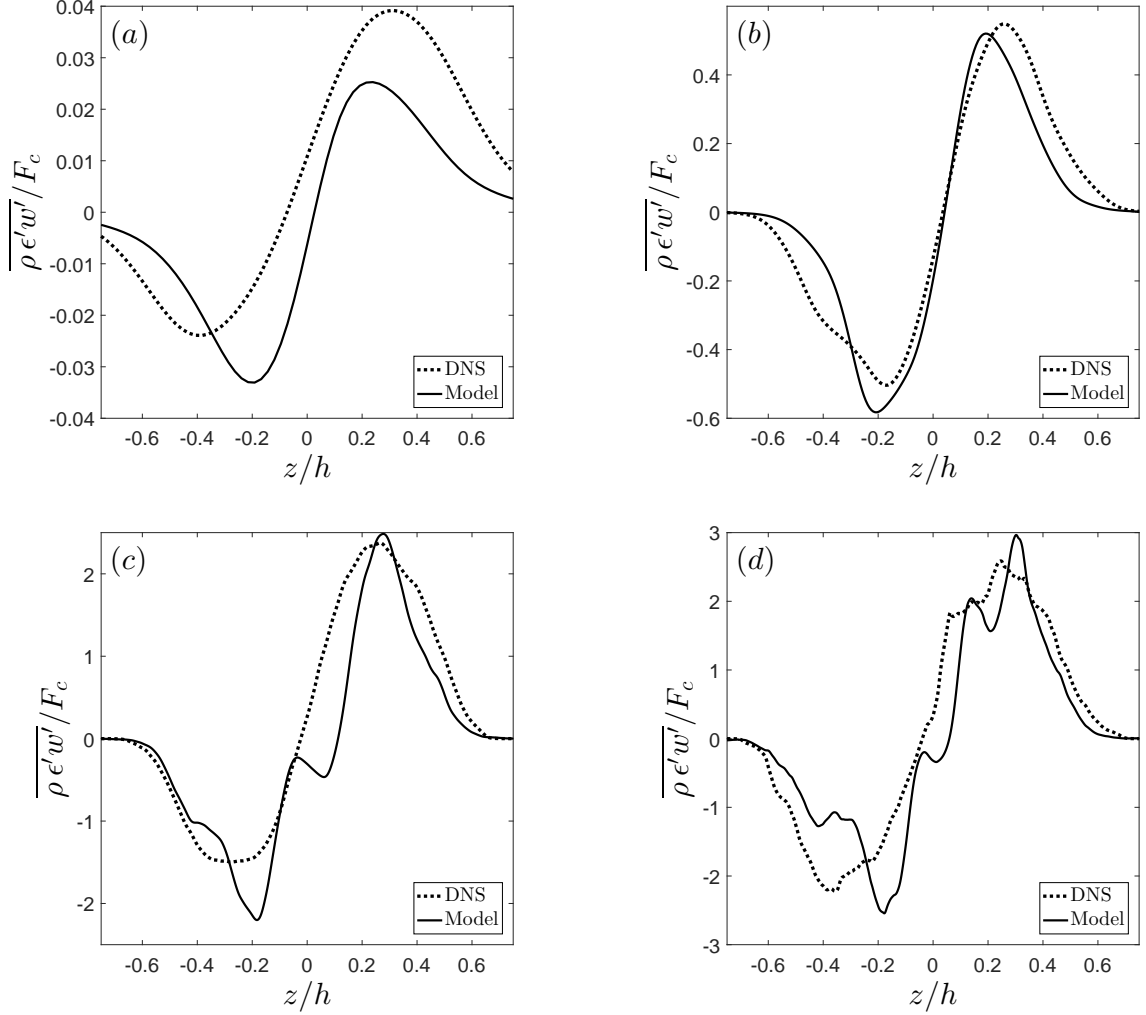
FIG. 9: Profiles of the vertical turbulent kinetic energy dissipation rate flux $\overline{\rho \epsilon' w'}$ normalized by $F_c = \rho_c u_c^3/t_c$ and its gradient-diffusion closure (26) at (a) $t/t_c = 5.13$, (b) 12.6, (c) 25.1, and (d) 37.9.

that the pressure fluxes are aligned with the turbulent fluxes of $K$ and $\epsilon$. The maximum value of $C_{pu}$ is attained at $t/t_c \approx 12.6$, corresponding to the time at which the molecular mixing parameter $\theta$ attains its minimum.[2] Once a Reynolds number $\mathrm{Re}_h^{\dot h} \approx 1,500$ has been attained, the coefficient for the pressure flux of $K$ approaches $C_{pu} \approx 0.2$. As shown in Fig. 9, the turbulent flux of $\epsilon$ becomes more important with increasing $\mathrm{Re}_h^{\dot h}$, while the pressure flux of $\epsilon$ remains relatively unchanged in magnitude. Thus, $C_{pu}^\epsilon$ decreases with increasing $\mathrm{Re}_h^{\dot h}$—at sufficiently large Reynolds numbers, the pressure flux of $\epsilon$ may be negligible compared with the turbulent flux. Table III gives $C_{pu}$ and $C_{pu}^\epsilon$ at various times.

### F. Similarity closures

Similarity closures used to phenomenologically model the non-flux, higher order correlations in the turbulent dissipation rate and scalar variance ($\epsilon$, $S$, and $\chi$) transport equations are examined here.

#### 1. The turbulent kinetic energy dissipation rate production and destruction terms

The buoyancy production of $\epsilon$ is the dominant production mechanism of $\epsilon$ for $t/t_c < 25.1$ and is non-negligible over the range of Reynolds numbers examined here[1]; this term is absent in constant density flows. The fluctuating velocity gradient–density gradient correlation is taken to be proportional to the buoyancy production of $K$, analogous to the similarity closure for the shear pro-
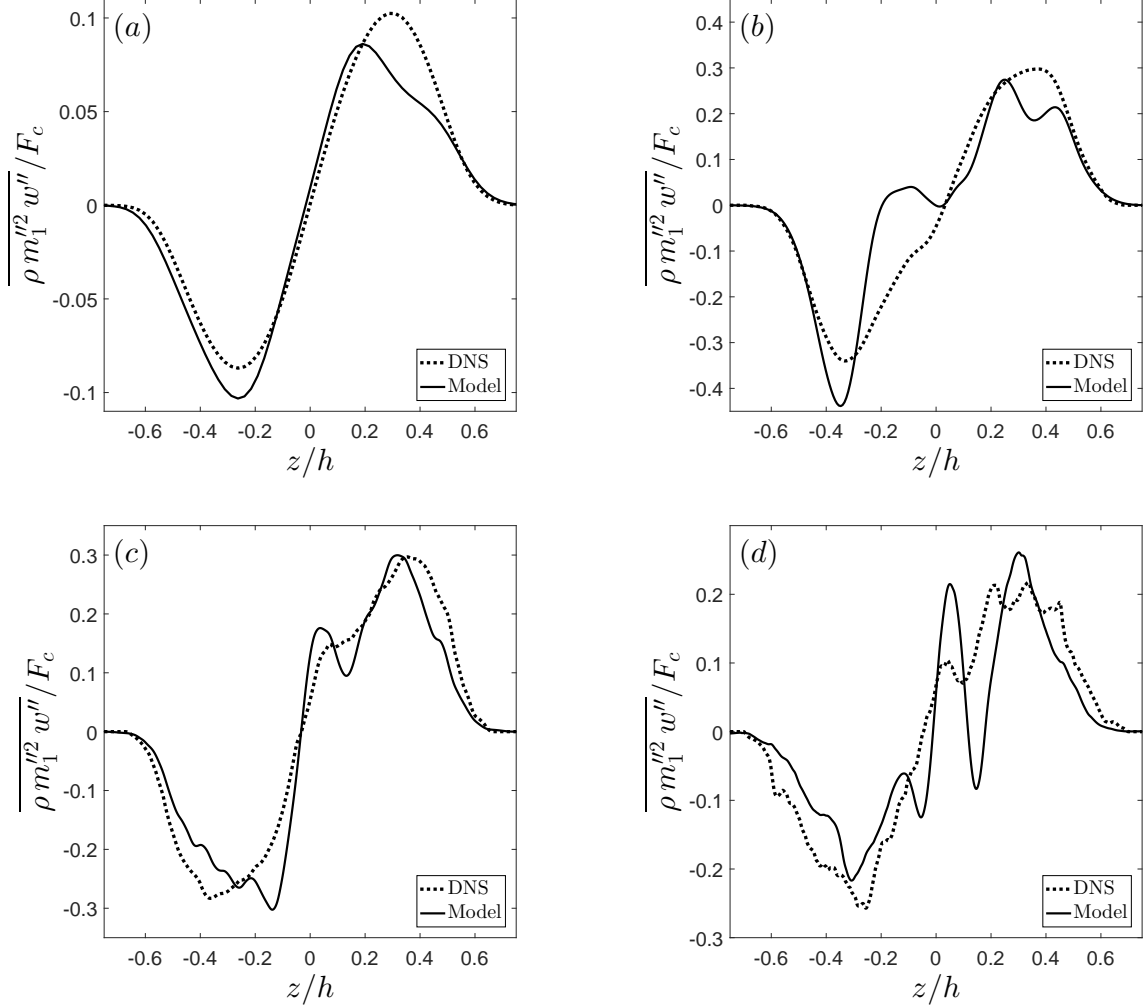
FIG. 10: Profiles of the vertical heavy-fluid mass fraction variance flux $\overline{\rho m_1''^2 w''}$ normalized by $F_c = \rho_c u_c$ and its gradient-diffusion closure (26) at (a) $t/t_c = 5.13$, (b) 12.6, (c) 25.1, and (d) 37.9.

duction rate of $\epsilon$,[24]

$$P_b^\epsilon = 2\,\overline{\nu}\,g_i\,\overline{\frac{\partial \rho'}{\partial x_j}\frac{\partial u_i'}{\partial x_j}} = C_{\epsilon 0}\,\frac{\epsilon}{K}\,P_b^K. \qquad (33)$$

Requiring the orders of magnitude to agree for the exact buoyancy production and its closure

$$P_b^\epsilon \sim -f\,\frac{\nu_t}{\overline{\rho}}\,\frac{\partial\overline{\rho}}{\partial z}\,\frac{\partial\overline{p}}{\partial z}\,\frac{\epsilon}{K} \sim f\,\frac{g\,\Delta\rho\,u_h^2}{h}$$

gives $f = \rho_{rms}/\Delta\rho$. The comparison of the exact and closed profiles of $P_b^\epsilon$ in Fig. 16 shows that the buoyancy production of $\epsilon$ is well-captured by similarity. However, because of the very small Atwood number, the profile of the exact shear production $P_s^\epsilon$ is very small and oscillatory.[1] Therefore, it is not possible to optimize the coefficient $C_{\epsilon 1}$ in the standard similarity model $P_s^\epsilon = C_{\epsilon 1}\,(\epsilon/K)\,P_s^K$ using the present data set.

The turbulent production and destruction of $\epsilon$ include triple fluctuating velocity gradient correlations and correlations of higher-order derivatives. Adopting the large Reynolds number closure,[8] the difference between the viscous destruction and turbulent production is

$$
\begin{aligned}
D^\epsilon - P_t^\epsilon &= 2\overline{\mu}\left[\overline{\nu\left(\frac{\partial^2 u_i'}{\partial x_j \partial x_k}\right)^2} + \overline{\frac{\partial u_i'}{\partial x_k}\frac{\partial u_i'}{\partial x_j}\frac{\partial u_k'}{\partial x_j}}\right] \quad (34) \\
&= C_{\epsilon 2}\,\frac{\overline{\rho}\,\epsilon^2}{K}.
\end{aligned}
$$

When there is no significant scale separation (as in the case here), the scale $\delta$ is approximately $\delta \sim \mathcal{O}(\lambda)$ rather than $\mathcal{O}(\ell_d)$ ($\ell_d$ is the Kolmogorov dissipation scale), so that requiring the orders of magnitude to agree for the exact turbulent destruction and its closure

$$D^\epsilon \sim f\,\frac{\overline{\rho}\,\epsilon^2}{K} \sim f\,\frac{\overline{\mu}\,\overline{\nu}\,u_h^2}{\lambda^4}$$
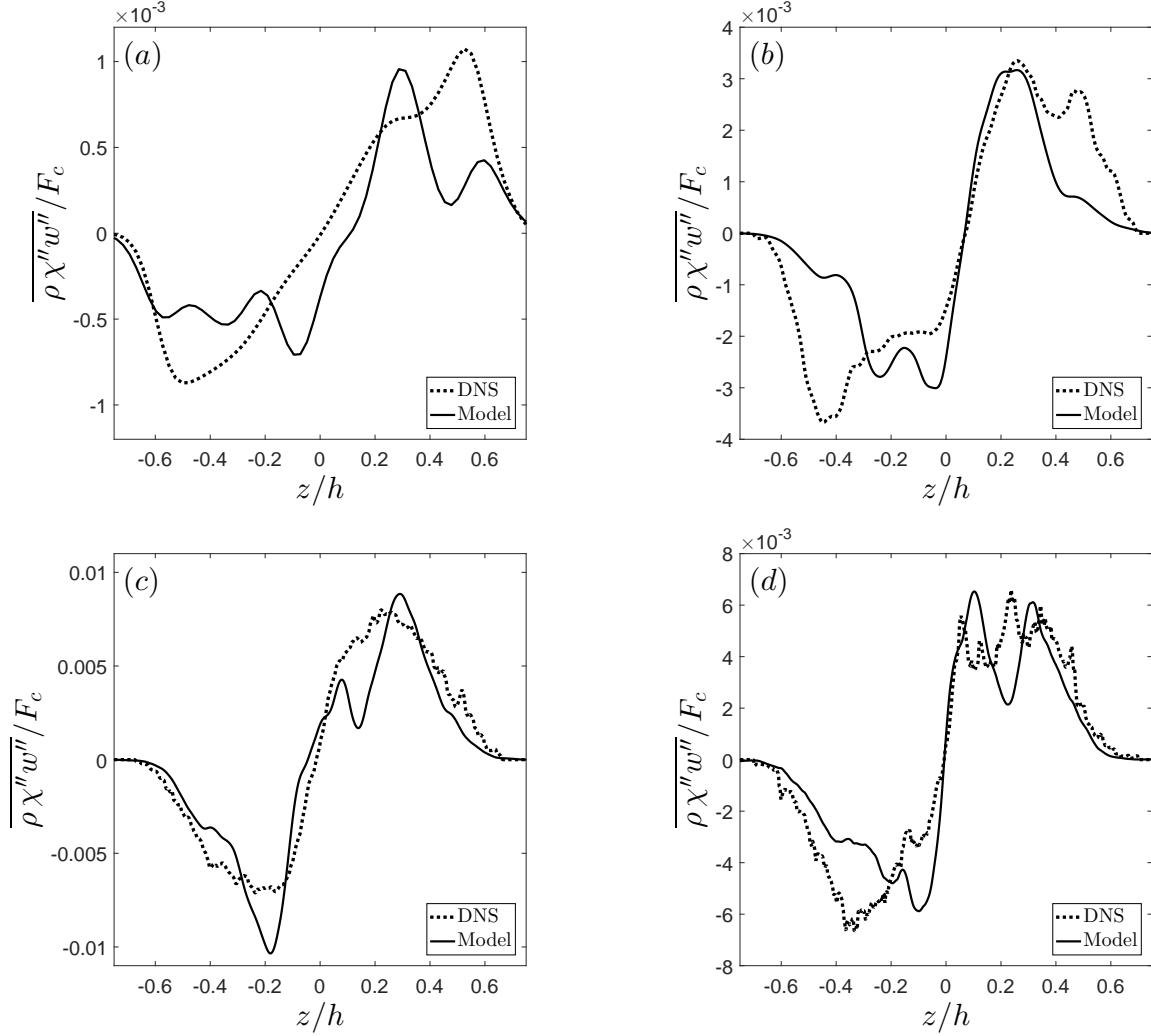
FIG. 11: Profiles of the vertical heavy-fluid mass fraction variance dissipation rate flux $\widetilde{\rho\chi''w''}$ normalized by $F_c = \rho_c u_c/t_c$ and its gradient-diffusion closure (27) at (a) $t/t_c = 5.13$, (b) 12.6, (c) 25.1, and (d) 37.9.

gives $f = 1$. Similarly, at small Reynolds numbers, the characteristic vortex stretching rate is $h/u_h$, rather than $\lambda/u_h$, so that the exact turbulent production scales as

$$P_t^\epsilon \sim \frac{\overline{\rho}\,\epsilon}{\tau} \sim \frac{\overline{\mu}\,u_h^3}{\lambda^2\,h},$$

where $\tau = h/u_h$. Thus, $f = 1$, and $D^\epsilon - P_t^\epsilon \sim \overline{\rho}\epsilon^2/K$, and no additional scaling factors are expected in Eq. (34). Profiles of the exact and modeled difference $D^\epsilon - P_t^\epsilon$ are shown in Fig. 17, where it is evident that the model agrees well with the DNS on average.

The buoyancy production and turbulent production/dissipation models in Figs. 16 and 17 are shown using the optimal coefficients $C_{\epsilon0}(\mathrm{Re}_h)$ and $C_{\epsilon2}(\mathrm{Re}_h)$, which are shown in Fig. 18. The coefficient $C_{\epsilon0}$ varies before $t/t_c = 25.1$, after which a late-time steady value $C_{\epsilon0} \approx 1.43$ is attained. This is larger than the value $C_{\epsilon0} = 0.91$ determined from an *a posteriori* model evaluation[33] and $C_{\epsilon0} = 0.95$ used to model

Rayleigh–Taylor and Richtmyer–Meshkov instability-driven mixing.[34] However, these studies determined $C_{\epsilon0}$ *a posteriori* that gave predictions in accord with experimental data and assumed values of the turbulent Schmidt numbers, whereas the present work uses the $\epsilon$ transport equation budget to directly determine $C_{\epsilon0}$ for the first time.

The evolution of the coefficient for the combined turbulent production/destruction of $\epsilon$ is also shown in Fig. 18, where $C_{\epsilon2} \approx 2.8$ when the mixing enters the transitional regime at $t/t_c \approx 12.6$. As the Reynolds number increases, this coefficient decreases to $C_{\epsilon2} \approx 2.26$ at the latest time ($t/t_c = 37.9$), larger than the standard shear flow value 1.92. Thus, the Reynolds number may need to be large enough that a sufficient scale separation exists between the energy containing and dissipative scales for $C_{\epsilon0}$ and $C_{\epsilon2}$ to asymptote. At the latest time, the peak of the kinetic energy and dissipation spectra are only separated by approximately one decade of wave numbers.[44].
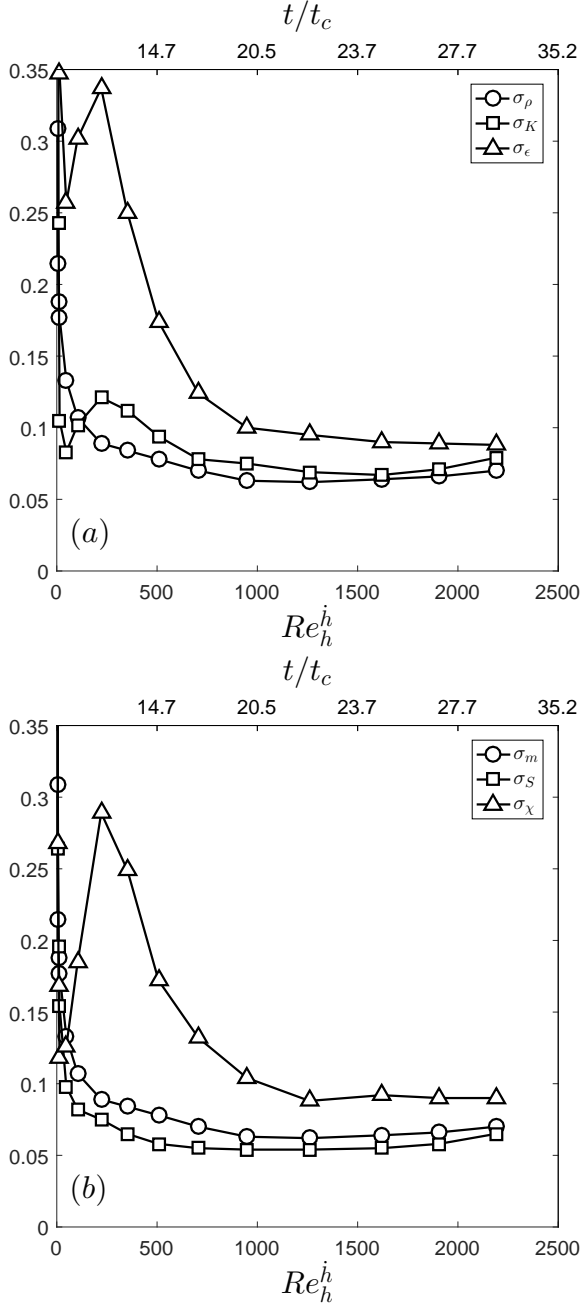
FIG. 12: Evolution of optimal (a) mechanical $\sigma_\rho$, $\sigma_K$, and $\sigma_\epsilon$ and (b) scalar $\sigma_m$, $\sigma_S$, and $\sigma_\chi$ turbulent Schmidt numbers.

Thus, $C_{\epsilon 2}$ is a weak function of $\mathrm{Re}_h$ until a broader scale separation is achieved. Both $C_{\epsilon 0}$ and $C_{\epsilon 2}$ attain maxima at $t/t_c \approx 17.3$ and decrease thereafter. Table III gives the values of the similarity coefficients $C_{\epsilon 0}$ and $C_{\epsilon 2}$ at various times.

### 2. The heavy-fluid mass fraction variance dissipation rate production and destruction terms

While similarity closures for the $\epsilon$ transport equation have been utilized for a large variety of flows, the modeling of the $S$ and $\chi$ transport equations has been primarily relegated to reacting flow and combustion applications.[51, 55, 56] The production of $S$, physically-represented by the entrainment of unmixed fluid, is determined by the product of the turbulent mass fraction flux $\widetilde{m_1'' w''}$ and the mean gradient $\partial \widetilde{m}_1/\partial x_j$. However, the higher-order correlation of fluctuating mass fraction gradients governing the destruction of $S$ (represented by molecular mixing of fluids across a species interface) does not have a gradient-diffusion closure. Instead, the relationship between the turbulent mechanical time scale $\tau_m = K/\epsilon$ and the scalar time scale $\tau_s = S/\epsilon_S$ is used to algebraically (rather than differentially) model the heavy-fluid mass fraction variance dissipation rate

$$\epsilon_S = 2\,\chi = 2\,C_\chi\,\frac{\epsilon}{K}\,S\,, \qquad (35)$$

where $C_\chi$ is a dimensionless coefficient.[5, 55–58] Requiring the orders of magnitude to agree for the mass fraction variance dissipation rate and its closure

$$\chi \sim f\,\frac{\epsilon}{K}\,S \sim f\,\frac{\overline{\nu}\,m_{rms}^2}{\lambda^2}$$

gives $f = \mathrm{Sc}^{-1}\,(\lambda/\lambda_m)^2 = 1$. In combustion applications, the role of the mass fraction variance is played by the mixture fraction variance. Using the time scale generalized by a Schmidt number-dependent contribution for scalars[56]

$$\tau_m = \frac{3\,K}{2\,\epsilon} + \sqrt{\frac{\overline{\nu}}{\epsilon}}\,\frac{\ln \mathrm{Sc}}{2} \qquad (36)$$

instead of Eq. (35) results in the expression

$$\epsilon_S = 2\,C_\chi\,\frac{S}{\frac{3\,K}{2\,\epsilon} + \sqrt{\frac{\overline{\nu}}{\epsilon}}\,\frac{\ln \mathrm{Sc}}{2}}\,. \qquad (37)$$

Estimating $\sqrt{\overline{\nu}/\epsilon}\,\ln\mathrm{Sc}/2$ from the DNS values gives an $\approx 5\%$ correction to $(3/2)\,K/\epsilon$, so that such a generalization is only significant for large Schmidt number mixing (and the modification of the coefficient of $\tau_m$ by $3/2$ would only change the value of $C_\chi$). The correction to $(3/2)\,K/\epsilon$ for the $\mathrm{Sc} = 620$ case[11] is $\approx 10$–$25\%$ depending on the time and location within the mixing layer.

Profiles of the mechanical and scalar time scales across the mixing layer are shown in Fig. 19. Once the mixing layer transitions into the nonlinear phase ($t/t_c \geq 12.6$), the mechanical time scale profiles are approximately constant across the mixing layer ($|z/h| < 0.5$) for all times. Similarly, the scalar time scale profiles are approximately
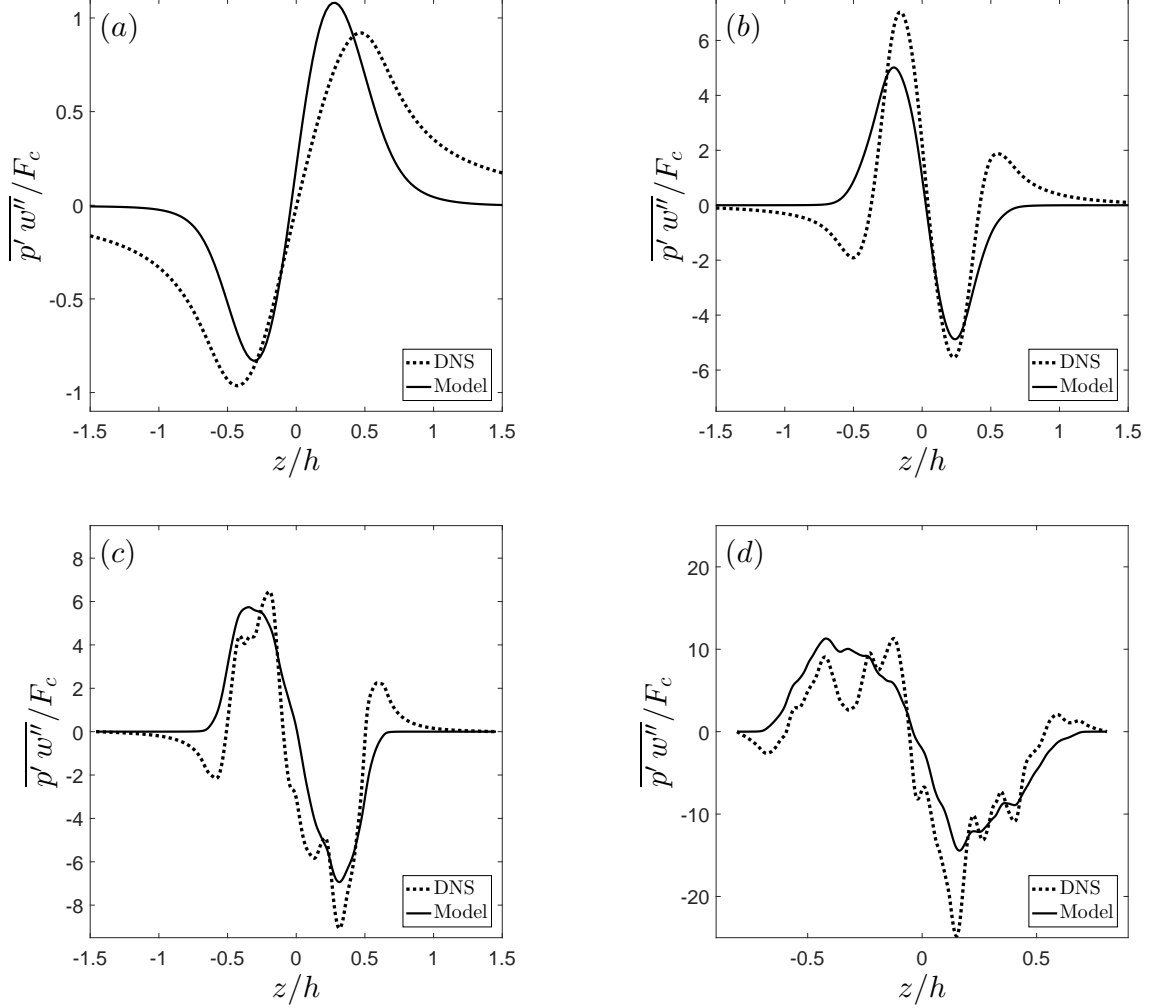
FIG. 13: Profiles of the vertical pressure flux $\overline{p'w''}$ normalized by $F_c = \rho_c u_c^3$ and the closure (31) at (a) $t/t_c = 5.13$, (b) 12.6, (c) 25.1, and (d) 37.9.

constant across the mixing layer only after the flow becomes transitional at $t/t_c \approx 17.3$. The mechanical-to-scalar time scale ratio is[15, 56, 59]

$$R = \frac{\tau_m}{\tau_s} = 2\,\frac{K}{\epsilon}\,\frac{\chi}{S}\,, \tag{38}$$

where Eqs. (35) and (37) give $C_\chi = R/2$ and $C_\chi = R\left(3 + \sqrt{\overline{\nu}\epsilon}\ln \mathrm{Sc}/K\right)/2$, respectively. Profiles of $R$ are shown in Fig. 20: $R$ is approximately constant across the mixing layer except near the layer boundaries, indicating that the algebraic closure (37) is a good approximation for this flow.[60] The profiles in Fig. 20 show a continuous increase in $R$ with time (and $\mathrm{Re}_h$). Many mixing models assume that this ratio is constant, with a value $R \approx 2$.[33, 46, 58] At the latest time in the simulation, $R \approx 0.9$–1.3 across the layer, which is considerably lower than the predicted values $R \approx 2.0$–2.2 using a spectral relaxation model developed for reacting flows.[56] At earlier times, the DNS gives $0.3 < R < 0.5$.

Profiles of the exact and closed heavy-fluid mass fraction variance destruction [using the algebraic model (37)]

$$D^S = \overline{\rho}\,\epsilon_S = 2\,\overline{\rho}\,\chi = 2\,C_\chi\,\frac{\overline{\rho}\,S}{\frac{3\,K}{2\,\epsilon} + \sqrt{\frac{\overline{\nu}}{\epsilon}}\,\frac{\ln \mathrm{Sc}}{2}} \tag{39}$$

are shown in Fig. 21. At early times ($t/t_c \leq 12.6$), the model exhibits adequate agreement with the DNS profiles. As the mixing layer becomes more turbulent, the agreement improves, as seen at $t/t_c = 25.1$ and 37.9. The detailed structure is not well captured by the model, except at $t/t_c = 25.1$. Using the model (35) instead gives similarly good agreement with the data. The evolution of the coefficient $C_\chi(\mathrm{Re}_h)$ used to construct the model profiles is shown in Fig. 25.

The fidelity of a RANS model may be improved by solving a transport equation for $\chi$, rather than using an algebraic model (35), as adopted in many reacting flow studies.[31, 51, 56, 61] The $\chi$ transport equation (like
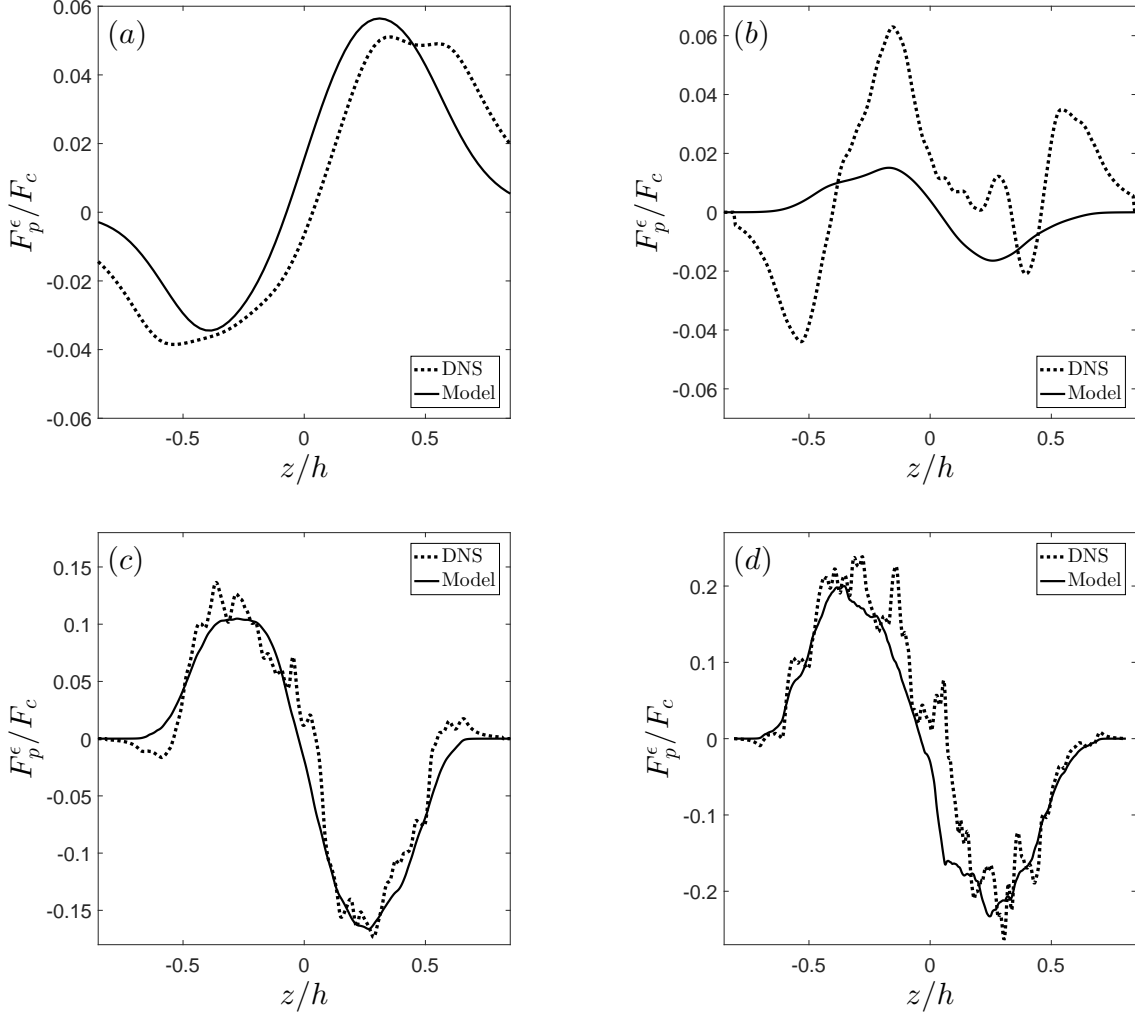
FIG. 14: Profiles of the pressure flux $F_p^\epsilon$ normalized by $F_c = \rho_c u_c^3/t_c$ and the closure (32) at (a) $t/t_c = 5.13$, (b) 12.6, (c) 25.1, and (d) 37.9.

that for $\epsilon$) contains higher order correlations which can not be closed by gradient-diffusion, and similarity must again be invoked. The mean production of $\chi$ is closed by[62, 63]

$$
\begin{aligned}
P_m^\chi &= -2\,\overline{\overline{D}\,\rho\,\frac{\partial m_1''}{\partial x_i}\frac{\partial u_j''}{\partial x_i}}\,\frac{\partial \widetilde{m}_1}{\partial x_j} \qquad (40)\\
&= C_{\chi 0}\,\frac{\mu_t}{\sqrt{\mathrm{Sc}}}\,\frac{\epsilon}{K}\left(\frac{\partial \widetilde{m}_1}{\partial x_j}\right)^2\\
&\longrightarrow C_{\chi 0}\,\frac{\mu_t}{\sqrt{\mathrm{Sc}}}\,\frac{\epsilon}{K}\left(\frac{\partial \widetilde{m}_1}{\partial z}\right)^2,
\end{aligned}
$$

where $C_{\chi 0}$ is a dimensionless coefficient and $\sigma_m$ has been absorbed into $C_{\chi 0}$. Using the estimate $D_t \sim \nu_t$, the Schmidt number scaling follows from requiring the orders of magnitude to agree for the exact mean production and

its closure

$$
P_m^\chi \sim f\,\overline{\rho}\,D_t\left(\frac{\partial \widetilde{m}_1}{\partial z}\right)^2\frac{\epsilon}{K} \sim f\,\frac{\overline{\mu}\,(\Delta m)^2\,u_h}{\lambda^2\,h}
$$

which gives $f = \mathrm{Sc}^{-1}\,(m_{rms}/\Delta m)(\lambda/\lambda_m) = (m_{rms}/\Delta m)/\sqrt{\mathrm{Sc}}$. Profiles of the exact and modeled heavy-fluid mean mass fraction variance gradient production are shown in Fig. 22. The model agrees well with the exact profiles, including the complex variations in the spatial structure. The oscillations in the model at later times are due to the gradient computed over the wide mixing layer with low effective resolution.

The mean production $P_m^\chi$ represents only a small fraction of the production of $\chi$, as the turbulent production $P_t^\chi$ is the dominant production mechanism. Similarly, the destruction of $\chi$ by molecular processes is also attributed to the fine-scale velocity fluctuations driving molecular mixing. In analogy with the closure of $D^\epsilon - P_t^\epsilon$,
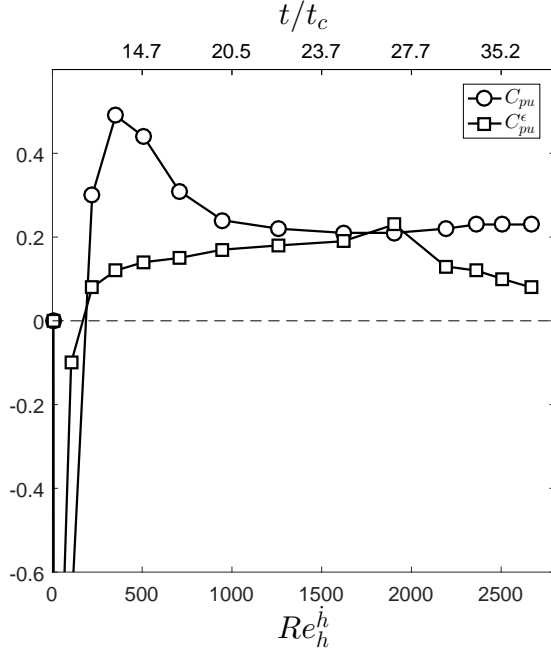
FIG. 15: Evolution of optimal pressure flux coefficients $C_{pu}$ and $C_{pu}^{\epsilon}$.

the difference of the turbulent destruction and production terms is modeled as[63, 64]

$$
\begin{aligned}
D^{\chi} - P_t^{\chi} &= 2\overline{D}^2 \overline{\rho \left( \frac{\partial^2 m_1''}{\partial x_i \partial x_j} \right)^2} \\
&\quad + 2\overline{D}\,\overline{\rho\, \frac{\partial m_1''}{\partial x_j} \frac{\partial m_1''}{\partial x_i} \frac{\partial u_j''}{\partial x_i}} \\
&= \sqrt{\mathrm{Re}_t}\,\overline{\rho}\,\chi \left( C_{\chi 2} \frac{\chi}{S} - C_{\chi 3} \frac{\epsilon}{K} \right),
\end{aligned}
\tag{41}
$$

where $C_{\chi 2}$ and $C_{\chi 3}$ are associated with $D^{\chi}$ and $P_t^{\chi}$, respectively. The $\sqrt{\mathrm{Re}_t}$ scaling follows from requiring that the orders of magnitude agree for the exact turbulent production and its closure

$$
P_t^{\chi} \sim f \frac{\overline{\rho}\,\chi^2}{S} \sim f \frac{\rho_0\, D^2\, m_{rms}^2}{\lambda_m^4},
$$

so that $f = \mathrm{Re}_\lambda \mathrm{Sc}(\lambda_m/\lambda)^2 \sim \sqrt{\mathrm{Re}_t}$. Similarly, requiring the orders of magnitude to agree for the exact turbulent destruction and its closure

$$
D^{\chi} \sim f \frac{\overline{\rho}\,\chi\,\epsilon}{K} \sim f \frac{\overline{\mu}\, D\, m_{rms}^2}{(\lambda\,\lambda_m)^2}
$$

gives $f \sim \sqrt{\mathrm{Re}_t}$. Profiles of the modeled and exact $P_t^{\chi}$ and $D^{\chi}$ are shown in Figs. 23 and 24, respectively. While the modeled $D^S$ shown in Fig. 21 is valid for $t/t_c > 5.13$, the turbulent production and destruction closures do not capture the flow physics until the transition to a pre-turbulent nonlinear stage at $t/t_c \approx 12.6$: both models fail to reproduce the structure of the DNS profiles at

$t/t_c = 5.13$. However, once turbulence ensues, the $P_t^{\chi}$ and $D^{\chi}$ closures agree very well with the DNS.

The evolution of the similarity coefficients for the $S$ and $\chi$ transport equations is shown in Fig. 25. The coefficient $C_{\chi 0}$ increases rapidly during the transient period, reaching a maximum of $\sim 9.3$ at $t/t_c \sim 20$, and then decreases to $\sim 6.8$ at the latest times. Both $C_\chi$ and $C_{\chi 3}$ increase from small values and nearly plateau beyond $t/t_c \sim 20$ at values $\sim 0.45$ and $\sim 0.72$, respectively. The coefficient $C_{\chi 2}$ decreases from a large value and varies relatively slowly beyond $t/t_c \sim 20$, attaining $\sim 1.30$ at the latest time. An implication of the time-evolution of $C_\chi$ is that the quantity governing the mixing rate $\chi$ is not steady, as often assumed.[34, 46, 58] Instead, there is a Reynolds number dependence over the flow evolution. Table III gives the values of the coefficients $C_\chi$, $C_{\chi 0}$, $C_{\chi 2}$, and $C_{\chi 3}$ at various times.

## IV. DISCUSSION AND CONCLUSIONS

A $1152 \times 760 \times 1280$ DNS dataset[2] corresponding to a model of a water channel Rayleigh–Taylor mixing experiment[3] was used to obtain and optimize coefficients for a three-equation $K$–$\epsilon$–$S$ or four-equation $K$–$\epsilon$–$S$–$\chi$ RANS model that generally provides a high degree of correlation between the exact terms and their gradient-diffusion or similarity closures *a priori*. In this data-driven approach, an $L_2$-norm [see Eq. (4)] minimization procedure between the exact and closed terms was used to compute Reynolds number-dependent turbulent Schmidt numbers and similarity coefficients. Correlation and amplitude coefficients, $r$ and $a$, [Eqs. (5) and (7)] given in the Appendix were computed for each pair of exact and closed terms to quantify how well the *shapes* and the *values* of the profiles agreed, respectively. Profiles were compared at dimensionless times, $t/t_c = 5.13$, 12.6, 25.1, and 37.9 [corresponding to $\mathrm{Re}_h^{\dot{h}} = (h\, dh/dt)/\overline{\nu} = 47$, 352, 1620, and 2666], representative of the linear, non-linear transitional, strongly nonlinear, and weakly turbulent flow regimes.[1, 2, 44] The model profiles exhibited increasing intermittent spatial variations as the Reynolds number increased, due to the decreasing number of turbulent structures over which averages are computed. Only terms contributing significantly to the budgets of the transport equations were examined.

An extension of the Boussinesq model that includes contributions from mean density and pressure gradients [Eq. (15)] was shown to adequately predict the diagonal Reynolds stresses. Gradient-diffusion models for the vertical turbulent fluxes $\widetilde{\overline{\rho}\phi_\alpha''w''}$ [Eqs. (25)–(27)] and pressure fluxes [Eqs. (31) and (32)] in the turbulent transport terms were examined with their corresponding turbulent Schmidt numbers determined by the $L_2$-norm minimization. The shapes and magnitudes of the exact and closed turbulent fluxes were in good agreement (modulo late-time oscillations in the models). The locations of maxima and minima were also in good agreement, except
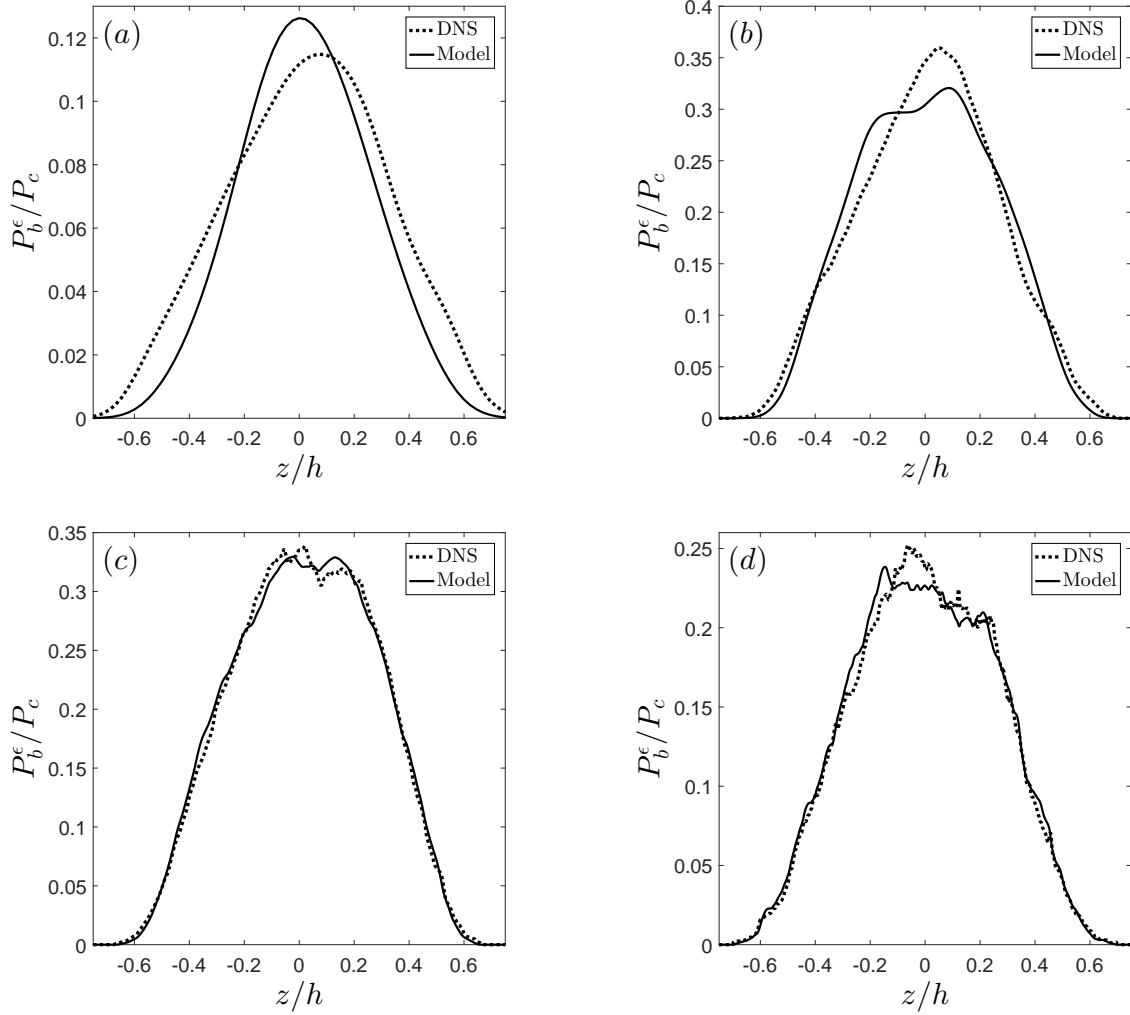
FIG. 16: Profiles of the buoyancy production $P_b^\epsilon$ normalized by $P_c = \rho_c u_c^2/t_c^2$ and its similarity closure (33) at (a) $t/t_c = 5.13$, (b) 12.6, (c) 25.1, and (d) 37.9.

at the latest time. Over the times considered, $\sigma_\epsilon$ and $\sigma_\chi$ exhibited the most variation. On average, $\sigma_\rho$, $\sigma_K$, $\sigma_m$, and $\sigma_S$ varied the least over the evolution: following the transient in $\sigma_\epsilon$ ($t/t_c \gtrsim 17.3$), these coefficients varied from $\approx 0.07$–$0.15$. In general, both $r$ and $a$ increased rapidly to near unity over $t/t_c \approx 2.6$–$17.3$ and then slowly decreased to $\approx 0.8$–$0.95$ for $t/t_c \gtrsim 17.3$ indicating good agreement. The shapes and magnitudes of the exact and closed pressure fluxes[28] were also in generally good agreement, together with the locations of the maxima and minima. The coefficients $C_{pu}$ and $C_{pu}^\epsilon$ changed sign at $t/t_c \approx 7.19$ due to the qualitative change in the flux profiles at this time[1]; $C_{pu}$ attains a maximum at $t/t_c \approx 12.6$ and then decreases to $\approx 0.22$ at late time, while $C_{pu}^\epsilon$ varies less with time. Both $r$ and $a$ are small at early and intermediate times, reaching $0.9$–$1.0$ for $t/t_c \gtrsim 17.3$ indicating that the pressure flux closure is more applicable to the large Reynolds number regime. The use of variable turbulent Prandtl and Schmidt num-

bers here is similar to the two-equation turbulence model with variable turbulent Schmidt and Prandtl numbers for scramjet supersonic mixing applications.[65–67]

Similarity models for the production and destruction terms (33)–(35) and (39)–(41) in the dissipation rate equations were examined with their coefficients determined by the $L_2$-norm minimization. These models capture both the shapes and values of the production terms $P_b^\epsilon$, $P_m^\chi$, and $P_t^\chi$ quite well (except for $P_t^\chi$ at the earliest time). Similarly, the shapes and values of $D^\epsilon - P_t^\epsilon$, $D^S$, and $D^\chi$ are also captured quite well by the models (except for $D^\chi$ at the earliest time). The models capture the maxima and other variations in the profiles accurately, yielding $r, a \approx 1$ for $t/t_c \gtrsim 10.1$. Both $C_{\epsilon 0}$ and $C_{\epsilon 2}$ increase fairly rapidly to maximum values at $t/t_c \approx 17.3$ and then decrease relatively slowly. Both $C_\chi$ and $C_{\chi 2}$ increase from small values and nearly plateau beyond $t/t_c \sim 20$. The coefficient $C_{\chi 0}$ increases rapidly, reaching a maximum at $t/t_c \sim 20$, and then decreases. The
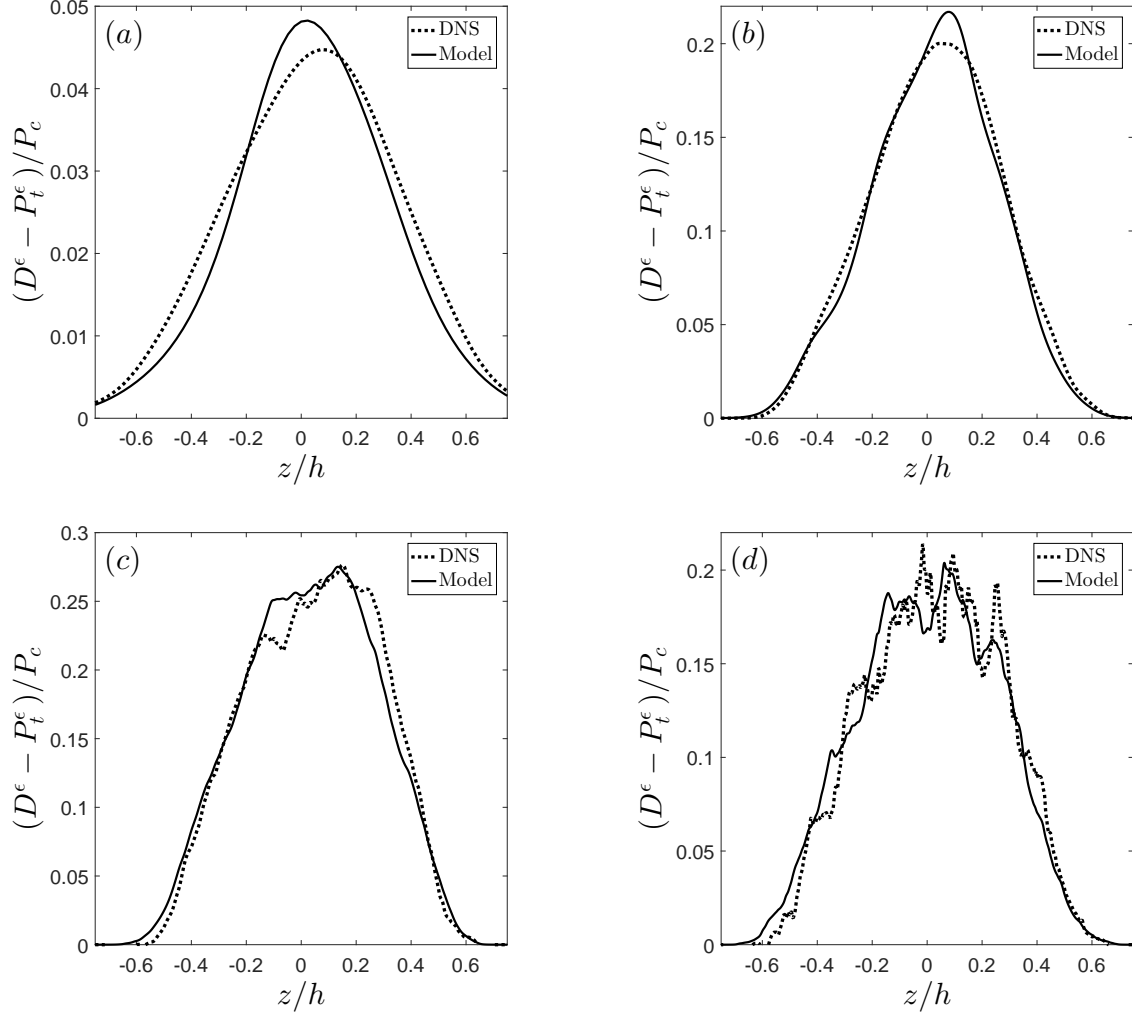
FIG. 17: Profiles of the difference between the turbulent kinetic energy dissipation rate destruction and production $D^\epsilon - P_t^\epsilon$ normalized by $P_c = \rho_c u_c^2 / t_c^2$ and its similarity closure (34) at (a) $t/t_c = 5.13$, (b) 12.6, (c) 25.1, and (d) 37.9.

coefficient $C_{\chi 3}$ decreases from a large value and varies relatively slowly beyond $t/t_c \sim 20$, attaining $\sim 1.30$ at the latest time. This study does not provide an optimized value of $C_{\epsilon 1}$ in the similarity model $P_s^\epsilon = C_{\epsilon 1} \left( \epsilon/K \right) P_s^K$; however, a standard value $C_{\epsilon 1} = 1.44$ may be a reasonable choice. A summary of the late-time coefficient values is given in Table II, and the Reynolds number-dependent coefficient values are given in Table III.

The present study suggests a RANS model for small Atwood number, intermediate Reynolds number Rayleigh–Taylor driven mixing based on the mean momentum and heavy-fluid mass fraction equations

$$\overline{\rho} \left( \frac{\partial}{\partial t} + \widetilde{u}_j \frac{\partial}{\partial x_j} \right) \widetilde{u}_i = \overline{\rho}\, g_i - \frac{\partial \overline{p}}{\partial x_i} + \frac{\partial \overline{\sigma}_{ij}}{\partial x_j} - \frac{\partial \tau_{ij}}{\partial x_j}, \quad (42)$$

$$\overline{\rho} \left( \frac{\partial}{\partial t} + \widetilde{u}_j \frac{\partial}{\partial x_j} \right) \widetilde{m}_1 = \frac{\partial}{\partial x_j} \left[ \left( \frac{\overline{\mu}}{\mathrm{Sc}} + \frac{\mu_t}{\sigma_m} \right) \frac{\partial \widetilde{m}_1}{\partial x_j} \right] \quad (43)$$

coupled to the four turbulence equations

$$\overline{\rho} \left( \frac{\partial}{\partial t} + \widetilde{u}_j \frac{\partial}{\partial x_j} \right) K = -\frac{\nu_t}{\sigma_\rho\, \overline{\rho}} \frac{\partial \overline{\rho}}{\partial x_j} \frac{\partial \overline{p}}{\partial x_j} - \tau_{ij} \frac{\partial \widetilde{u}_i}{\partial x_j} \quad (44)$$
$$- \overline{\rho}\, \epsilon + \frac{\partial}{\partial x_j} \left[ \left( \overline{\mu} + \frac{\mu_t}{\sigma_K^*} \right) \frac{\partial K}{\partial x_j} \right],$$

$$\overline{\rho} \left( \frac{\partial}{\partial t} + \widetilde{u}_j \frac{\partial}{\partial x_j} \right) \epsilon = -C_{\epsilon 0} \frac{\epsilon}{K} \frac{\nu_t}{\sigma_\rho\, \overline{\rho}} \frac{\partial \overline{\rho}}{\partial x_j} \frac{\partial \overline{p}}{\partial x_j} \quad (45)$$
$$- C_{\epsilon 1} \frac{\epsilon}{K} \tau_{ij} \frac{\partial \widetilde{u}_i}{\partial x_j} - C_{\epsilon 2} \frac{\overline{\rho}\, \epsilon^2}{K}$$
$$+ \frac{\partial}{\partial x_j} \left[ \left( \overline{\mu} + \frac{\mu_t}{\sigma_\epsilon^*} \right) \frac{\partial \epsilon}{\partial x_j} \right],$$
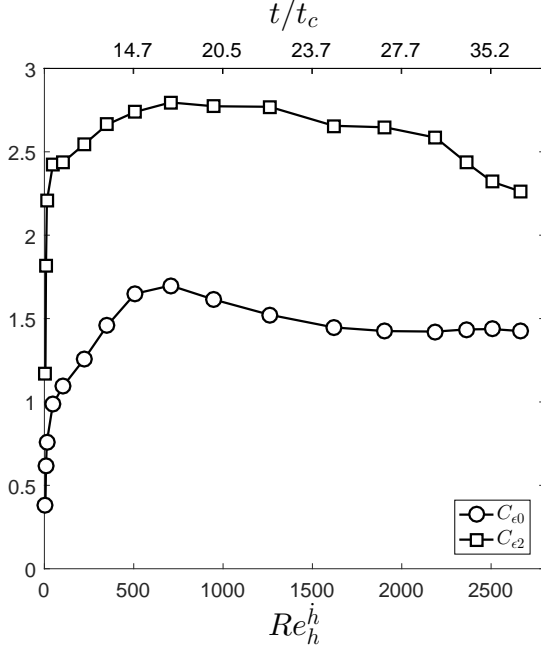
FIG. 18: Evolution of optimal similarity coefficients $C_{\epsilon 0}$ and $C_{\epsilon 2}$ in the $\overline{\epsilon'}$ transport equation.

$$\overline{\rho}\left(\frac{\partial}{\partial t} + \widetilde{u}_j \frac{\partial}{\partial x_j}\right)S = 2\frac{\mu_t}{\sigma_m}\left(\frac{\partial \widetilde{m}_1}{\partial x_j}\right)^2 - 2\overline{\rho}\chi \quad (46)$$
$$+ \frac{\partial}{\partial x_j}\left[\left(\frac{\overline{\mu}}{\text{Sc}} + \frac{\mu_t}{\sigma_S}\right)\frac{\partial S}{\partial x_j}\right],$$

$$\overline{\rho}\left(\frac{\partial}{\partial t} + \widetilde{u}_j \frac{\partial}{\partial x_j}\right)\chi = C_{\chi 0}\frac{\mu_t}{\sqrt{\text{Sc}}}\frac{\epsilon}{K}\left(\frac{\partial \widetilde{m}_1}{\partial x_j}\right)^2 \quad (47)$$
$$- \sqrt{\text{Re}_t}\,\overline{\rho}\,\chi\left(C_{\chi 2}\frac{\chi}{S} - C_{\chi 3}\frac{\epsilon}{K}\right)$$
$$+ \frac{\partial}{\partial x_j}\left[\left(\frac{\overline{\mu}}{\text{Sc}} + \frac{\mu_t}{\sigma_\chi}\right)\frac{\partial \chi}{\partial x_j}\right]$$

with coefficient values given in Table II, $\sigma_K^* = \sigma_K/(1 - C_{pu}) = 0.17$, and $\sigma_\epsilon^* = \sigma_\epsilon/\left(1 - C_{pu}^\epsilon\right) = 0.11$. The turbulent viscosity is (2) and the Reynolds stress is modeled using the buoyancy-generalized model in Eq. (15). The pairs $(K, \epsilon)$ and $(S, \chi)$ provide a mixing model describing *both mechanical and scalar mixing*, respectively. A three-equation model in which $\chi$ is modeled algebraically by Eq. (35) provides a simpler alternative model. Such models are analogous to those used in turbulent nonpremixed combustion, in which the scalar progress variables are the mixture fraction variance and its dissipation rate.[51, 55] Equations (44) and (45) were used in a reacting mixing layer study.[9] Equation (47) is similar to the equation used in the context of a second-order closure for momentum and passive scalar transport,[5, 15, 68] except that the gradient-diffusion model is used here for the turbulent diffusion,[63] rather than the generalized gradient-diffusion model, and the shear production $P_s^\chi$ is neglected here. A $K$–$\epsilon$–$\overline{T'^2}$–
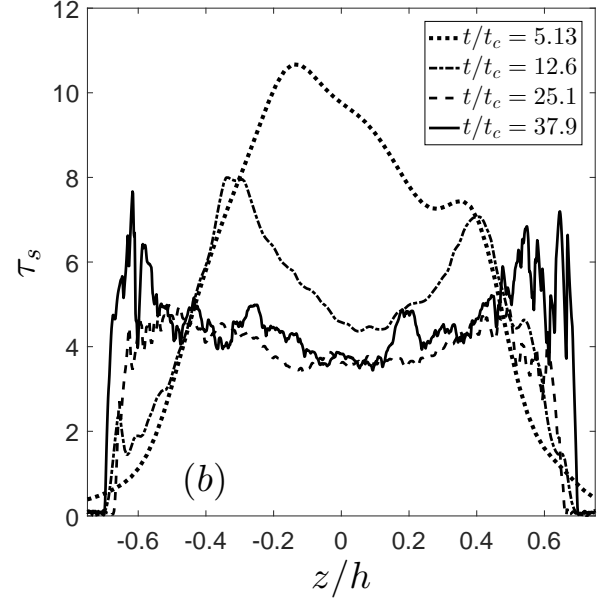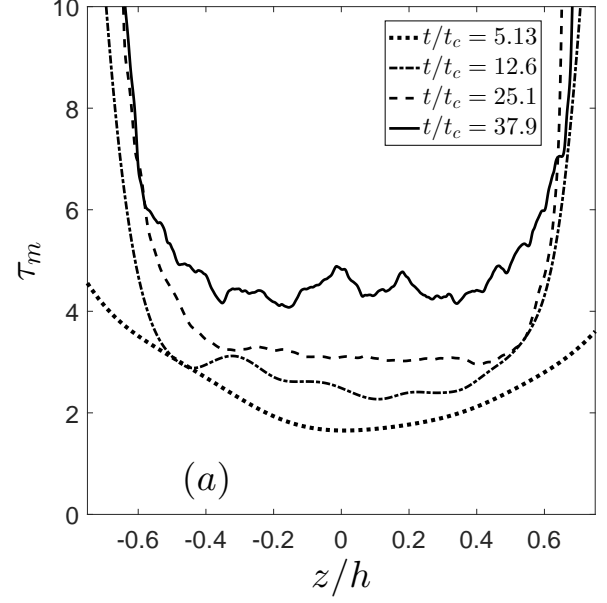


FIG. 19: Profiles of the (a) mechanical time scale $\tau_m$ and (b) scalar time scale $\tau_s$ at various dimensionless times.

$\epsilon_T$ model (where $\overline{T'^2}$ and $\epsilon_T$ are the temperature variance and its dissipation rate) was formulated for turbulent convection,[69, 70] and a $K$–$\epsilon$–$\overline{T'^2}$–$\epsilon_T$ model was used to investigate turbulence effects in buoyant diffusion flames.[71]

An important conclusion of this study is that, contrary to the implicit assumption of large Reynolds number and statistical isotropy embodied in gradient-diffusion and similarity closure models, very large Reynolds numbers are not required in Rayleigh–Taylor flows to achieve good agreement with such models. It was also demonstrated
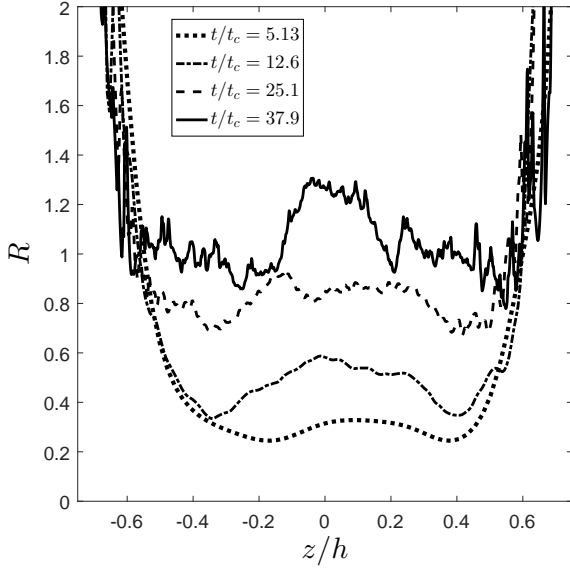
FIG. 20: Profile of the mechanical-to-scalar time scale ratio $R$ (38) at various dimensionless times.

that standard gradient-diffusion and similarity closures are remarkably accurate *a priori* at late times, provided that turbulent Reynolds number scalings are incorporated into the closures of the turbulent production and destruction in the mass fraction variance dissipation rate equation.

The model equations proposed here are likely to apply to other Rayleigh–Taylor unstable flows, but the optimized model coefficients are specific to the DNS data set analyzed here. For example, the early-time calibration of the model embodies the details of the initial conditions particular to the experiment modeled using the DNS.[2] The late-time calibration is also consistent with the relatively large value of $\alpha$ measured in the experiment, and will change if experiments with initial spectra different from the ones considered here are modeled (which may be consistent with a different late-time value of $\alpha$). While the coefficients vary most during early times when the production-to-dissipation (and destruction) ratios are largest, the closures nevertheless capture both the shape and magnitude of the DNS profiles reasonably well. As in the case of subgrid-scale model assessment for large-eddy simulation, good *a priori* predictions of a model do not necessarily imply equally good *a posteriori* predictions: the *a priori* optimized models suggested here are investigated *a posteriori* in a companion paper. The DNS data presented here can be used to motivate the development of small Reynolds number modifications of the closures to further improve their early-time predictions.

## Appendix: Correlation and amplitude coefficients

The correlation and amplitude coefficients corresponding to each gradient-diffusion and similarity closure model are given at various times in Tables IV and V, respectively. The generalized Boussinesq model (15) generally captures the shape and magnitude of $\widetilde{u''^2}$, $\widetilde{v''^2}$, and $\widetilde{w''^2}$ well, with the exception of the first time, as seen in the evolution of the correlation and amplitude coefficients. Beyond $t/t_c \approx 7.18$, $r \approx 0.75$–$0.94$ for $C_A^{(1111)}$, $r \approx 0.37$–$0.58$ for $C_A^{(2222)}$, and $r \approx 0.84$–$0.95$ for $C_A^{(3333)}$, showing that $\widetilde{u''^2}$ and $\widetilde{w''^2}$ correlate with the DNS relatively well, while $\widetilde{v''^2}$ generally does not correlate as well. Similar trends are seen in the amplitude coefficients, with $a \approx 1.02$–$1.18$ for $C_A^{(1111)}$, $a \approx 1.24$–$1.84$ for $C_A^{(2222)}$, and $a \approx 0.92$–$0.98$ for $C_A^{(3333)}$ for $t/t_c > 7.18$.

The turbulent flux closures shown in Figs. 7–11 show favorable agreement beyond $t/t_c > 5.13$, with $r, a > 0.9$ at most times. At the latest times ($t/t_c \gtrsim 29.8$), $r$ and $a$ decrease, which is attributable to the increase in oscillations in the profiles, and hence increased oscillations in the profile gradients required to construct the closures. To reduce these oscillations, a locally-weighted, linear, least-squares regression[72, 73] was applied to a 51-point stencil to filter the mean profiles before calculating gradients.

Before the early-time nonlinear transition at $t/t_c \approx 12.6$, both pressure flux closures shown in Figs. 13 and 14 capture the pressure transport given negative values of $C_{pu}$ and $C_{pu}^\epsilon$. During the nonlinear transition, $t/t_c \approx 7.18$–$10.1$ for $K$ and $t/t_c \approx 10.1$–$14.9$ for $\epsilon$, the correlation between the model and DNS substantially decreases. The model for the pressure transport of $K$ is adequate after the transition, while the model for the pressure transport of $\epsilon$ exhibits better agreement at $t/t_c > 25.1$, due to the negligible flux of $\epsilon$ away from the mixing layer boundaries that the model must capture.

Similarity models for the buoyancy production and turbulent production/destruction terms exhibit good agreement with the DNS after $t/t_c = 5.13$. The algebraic closure for $\chi$ agrees well with the DNS over all times when using the time-dependent values of $C_\chi$. Similarly, $P_m^\chi$ shows excellent agreement with the DNS over all Reynolds numbers. The turbulent production and destruction terms poorly correlate with the DNS until $t/t_c \approx 12.6$, after which turbulent fluctuations become more important, and the closures accurately reflect the flow physics.
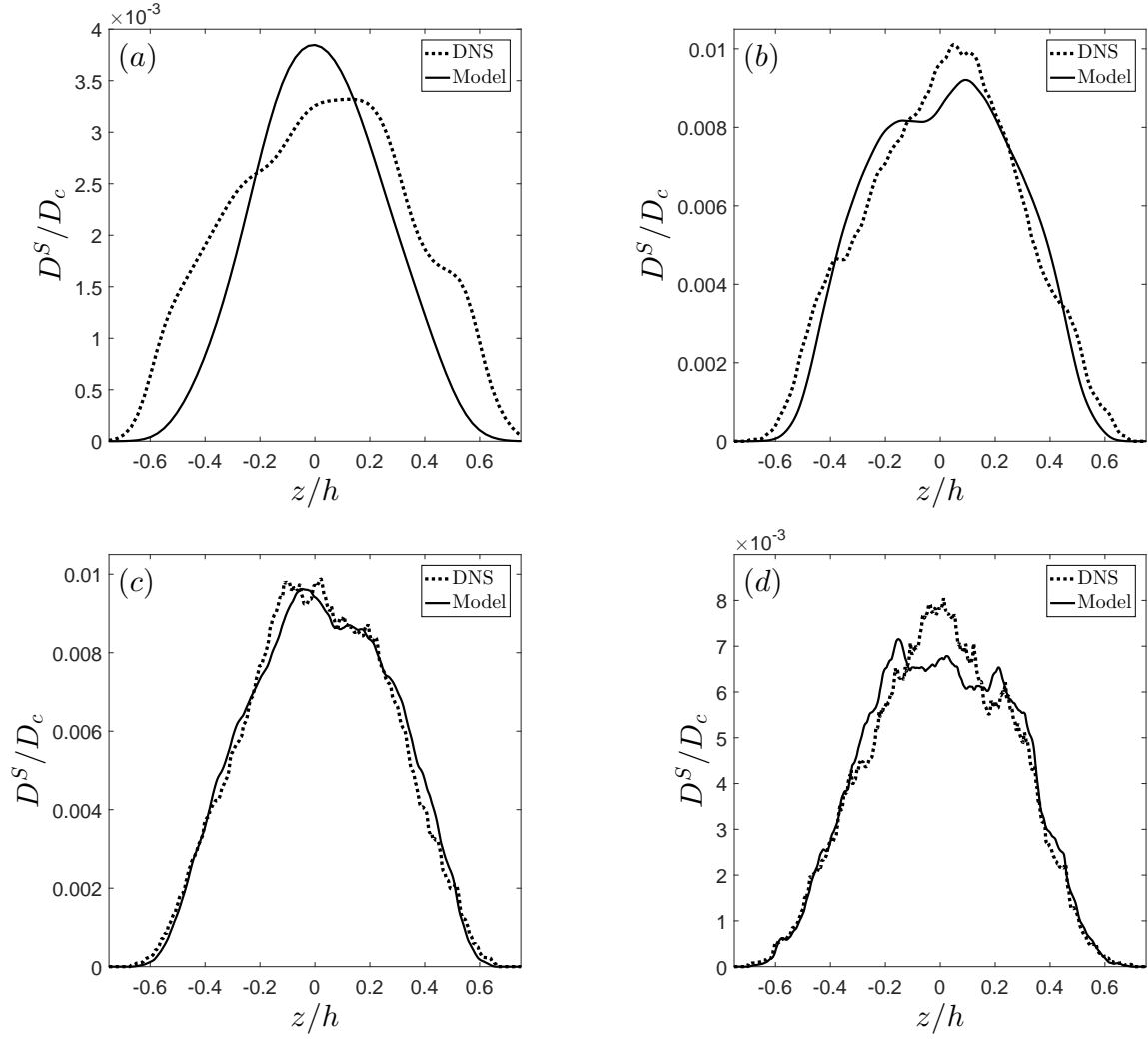
FIG. 21: Profiles of the heavy-fluid mass fraction variance destruction $D^S$ normalized by $D_c = \rho_c/t_c$ and its similarity closure (39) at (a) $t/t_c = 5.13$, (b) 12.6, (c) 25.1, and (d) 37.9.
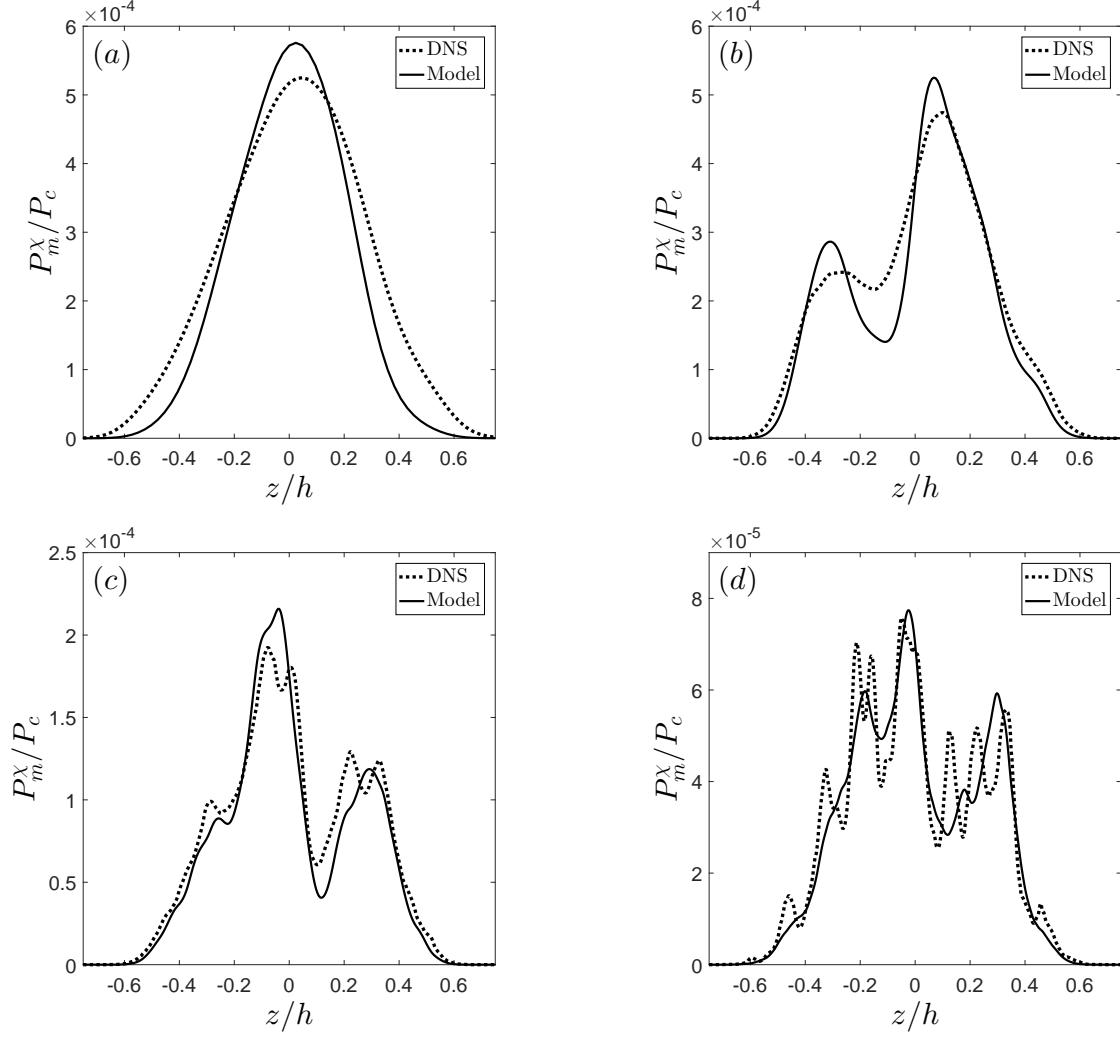
FIG. 22: Profiles of the heavy-fluid mass fraction variance dissipation rate mean production $P_m^\chi$ normalized by $P_c = \rho_c/t_c^2$ and its similarity closure (40) at (a) $t/t_c = 5.13$, (b) 12.6, (c) 25.1, and (d) 37.9.
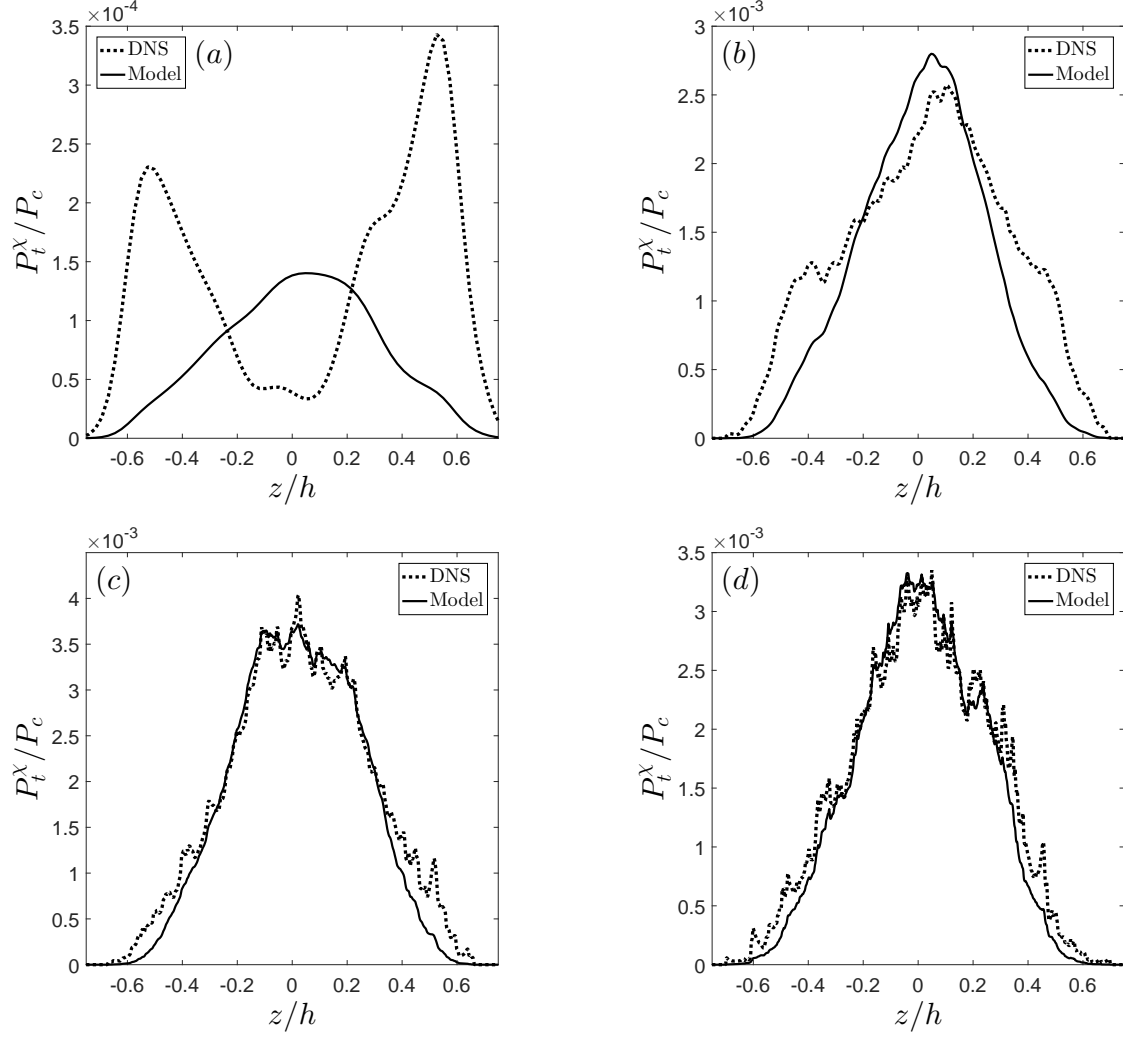
FIG. 23: Profiles of the heavy-fluid mass fraction variance dissipation rate turbulent production $P_t^\chi$ normalized by $P_c = \rho_c/t_c^2$ and its similarity closure at (a) $t/t_c = 5.13$, (b) 12.6, (c) 25.1, and (d) 37.9.
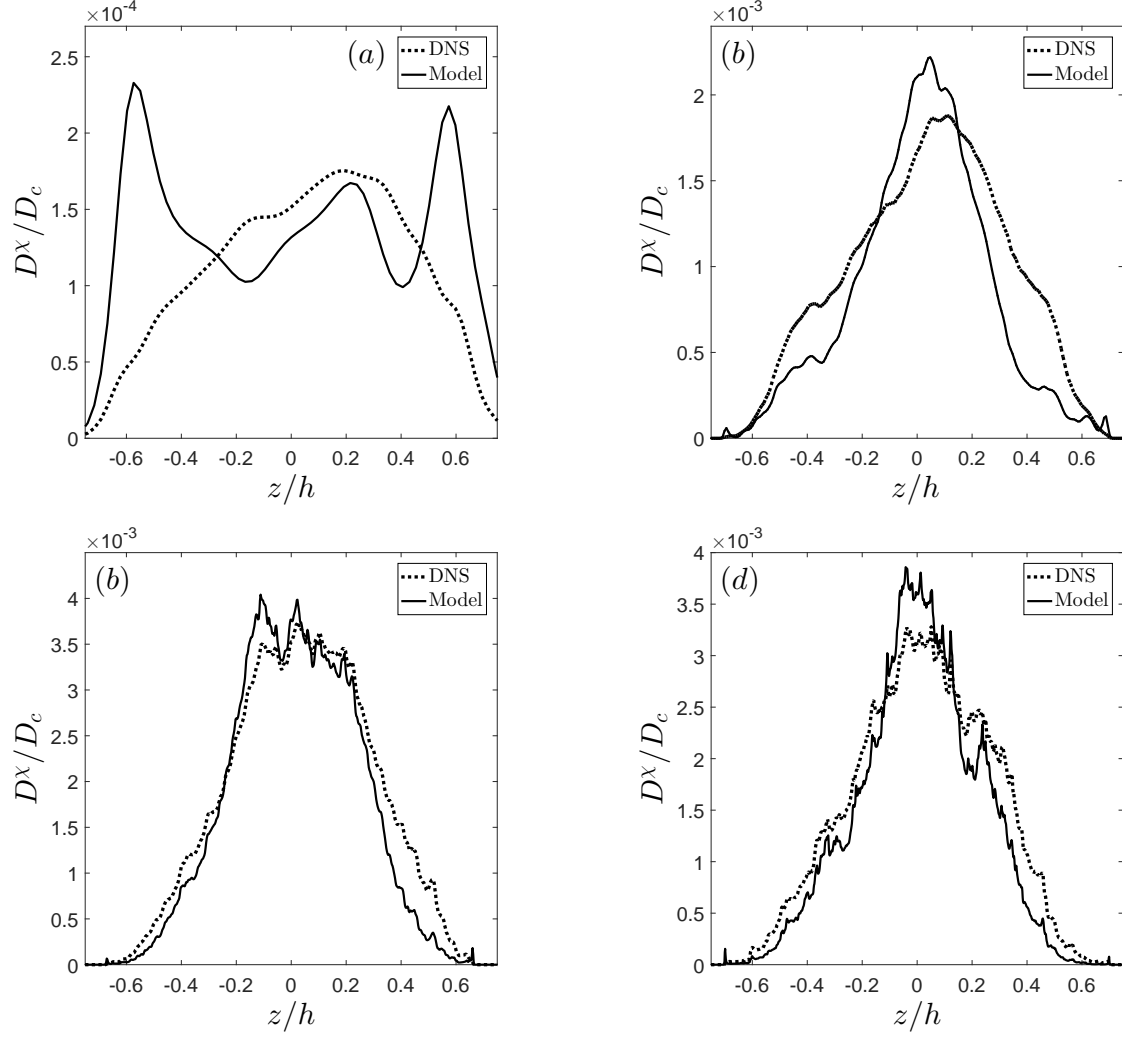
FIG. 24: Profiles of the heavy-fluid mass fraction variance dissipation rate destruction term $D^\chi$ normalized by $D_c = \rho_c/t_c^2$ and its similarity closure at (a) $t/t_c = 5.13$, (b) 12.6, (c) 25.1, and (d) 37.9.
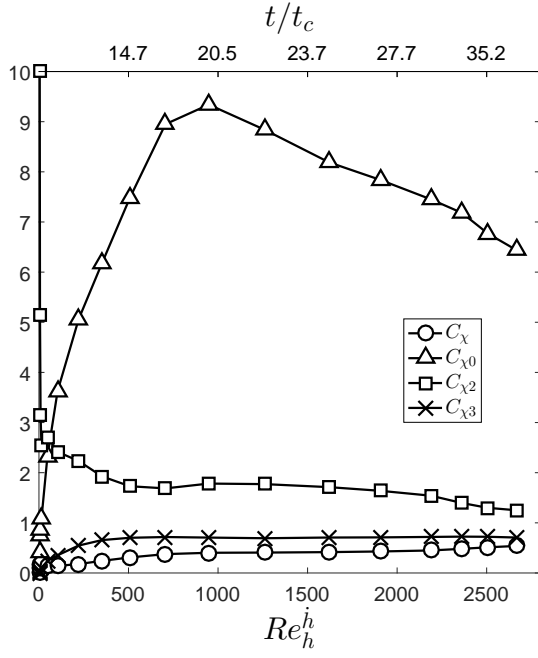
FIG. 25: Evolution of optimal similarity coefficients for the $S$ and $\chi$ transport equations.

| Coefficient | Closure | Value |
|:---:|:---:|:---:|
| $C_\mu$ | turbulent viscosity | 0.09 |
| $C_A^{(1111)}$ | Reynolds stress $\tau_{11}$ | $2.02^\dagger$ |
| $C_A^{(2222)}$ | Reynolds stress $\tau_{22}$ | $3.02^*$ |
| $C_A^{(3333)}$ | Reynolds stress $\tau_{33}$ | $2.63^\dagger$ |
| $\sigma_\rho$ | turbulent flux of $\rho'$ | $0.08^*$ |
| $\sigma_K$ | turbulent flux of $K''$ | $0.09^*$ |
| $\sigma_\epsilon$ | turbulent flux of $\epsilon'$ | $0.10^\dagger$ |
| $C_{pu}$ | pressure flux of $K''$ | 0.23 |
| $C_{pu}^\epsilon$ | pressure flux of $\epsilon'$ | $0.10^\dagger$ |
| $\sigma_m$ | turbulent flux of $m_1''$ | $0.08^*$ |
| $\sigma_S$ | turbulent flux of $m_1''^2$ | $0.07^*$ |
| $\sigma_\chi$ | turbulent flux of $\chi''$ | $0.15^*$ |
| $C_{\epsilon 0}$ | buoyancy production of $\epsilon$ | 1.44 |
| $C_{\epsilon 2}$ | turbulent dissipation of $\epsilon$ | $2.32^\dagger$ |
| $C_\chi$ | turbulent dissipation of $S$ | $0.51^*$ |
| $C_{\chi 0}$ | mean production of $\chi$ | 6.77 |
| $C_{\chi 2}$ | turbulent dissipation of $\chi$ | $1.30^\dagger$ |
| $C_{\chi 3}$ | turbulent production of $\chi$ | $0.72^\dagger$ |

TABLE II: Constant coefficients for the *a priori* optimized $K$–$\epsilon$–$S$–$\chi$ transport model for Rayleigh–Taylor turbulence proposed in the present study. An asterisk ($*$) or dagger ($\dagger$) indicates that the coefficient is slightly increasing or decreasing at late time, respectively.

| $t/t_c$ | $Re_h$ | $Re_t(z=0)$ | $C_A^{(1111)}$ | $C_A^{(2222)}$ | $C_A^{(3333)}$ | $\sigma_\rho$ | $\sigma_K$ | $\sigma_\epsilon$ | $C_{pu}$ | $C_{pu}^\epsilon$ | $\sigma_m$ | $\sigma_S$ | $\sigma_\chi$ | $C_{\epsilon 0}$ | $C_{\epsilon 2}$ | $C_\chi$ | $C_{\chi 0}$ | $C_{\chi 2}$ | $C_{\chi 3}$ |
|---|---|---|---|---|---|---|---|---|---|---|---|---|---|---|---|---|---|---|---|
| 0 | 4.4 | 0.0 | 0.00 | 0.00 | 0.00 | 0.31 | 7.14 | >10 | 0 | 0 | 0.31 | 0.40 | 0.41 | >10 | 1.06 | 0.01 | 0.42 | >10.0 | 0 |
| 0.85 | 5.8 | 0.3 | 0.00 | 0.46 | 0.21 | 0.22 | 0.52 | 0.55 | <−1 | <−1 | 0.22 | 0.26 | 0.27 | 0.38 | 1.17 | 0.10 | 0.76 | 5.15 | 0.02 |
| 1.71 | 9.0 | 0.6 | 0.00 | 0.57 | 0.41 | 0.19 | 0.24 | 0.44 | <−1 | <−1 | 0.19 | 0.20 | 0.17 | 0.62 | 1.82 | 0.17 | 0.87 | 3.14 | 0.04 |
| 2.57 | 14 | 1 | 0.17 | 0.74 | 0.66 | 0.18 | 0.11 | 0.35 | <−1 | <−1 | 0.18 | 0.15 | 0.12 | 0.76 | 2.21 | 0.18 | 1.08 | 2.54 | 0.09 |
| 5.13 | 47 | 5 | 0.66 | 1.18 | 1.16 | 0.13 | 0.08 | 0.26 | <−1 | −0.87 | 0.13 | 0.10 | 0.13 | 0.99 | 2.42 | 0.15 | 2.33 | 2.71 | 0.24 |
| 7.18 | 104 | 13 | 0.87 | 1.33 | 1.42 | 0.11 | 0.10 | 0.30 | −0.71 | −0.1 | 0.11 | 0.08 | 0.19 | 1.09 | 2.44 | 0.14 | 3.63 | 2.42 | 0.35 |
| 10.1 | 222 | 38 | 1.12 | 1.48 | 1.86 | 0.09 | 0.12 | 0.34 | 0.30 | 0.08 | 0.09 | 0.08 | 0.29 | 1.26 | 2.54 | 0.18 | 5.06 | 2.23 | 0.55 |
| 12.6 | 352 | 62 | 1.21 | 1.77 | 2.28 | 0.08 | 0.11 | 0.25 | 0.49 | 0.12 | 0.08 | 0.07 | 0.25 | 1.46 | 2.66 | 0.24 | 6.18 | 1.93 | 0.66 |
| 14.9 | 508 | 69 | 1.33 | 2.61 | 2.90 | 0.08 | 0.09 | 0.17 | 0.44 | 0.14 | 0.08 | 0.06 | 0.17 | 1.65 | 2.74 | 0.31 | 7.48 | 1.73 | 0.70 |
| 17.3 | 706 | 76 | 1.70 | 4.77 | 3.59 | 0.07 | 0.08 | 0.12 | 0.31 | 0.15 | 0.07 | 0.06 | 0.13 | 1.70 | 2.80 | 0.38 | 8.95 | 1.69 | 0.72 |
| 20.0 | 948 | 90 | 2.57 | 5.16 | 4.30 | 0.06 | 0.08 | 0.10 | 0.24 | 0.17 | 0.06 | 0.05 | 0.10 | 1.61 | 2.77 | 0.40 | 9.34 | 1.78 | 0.71 |
| 22.5 | 1260 | 115 | 2.96 | 5.02 | 4.36 | 0.06 | 0.07 | 0.10 | 0.22 | 0.18 | 0.06 | 0.05 | 0.09 | 1.52 | 2.77 | 0.41 | 8.84 | 1.77 | 0.69 |
| 25.1 | 1620 | 154 | 2.88 | 4.42 | 4.00 | 0.06 | 0.07 | 0.09 | 0.21 | 0.19 | 0.06 | 0.06 | 0.09 | 1.45 | 2.66 | 0.42 | 8.19 | 1.71 | 0.71 |
| 27.4 | 1905 | 194 | 2.78 | 4.31 | 3.72 | 0.07 | 0.07 | 0.09 | 0.21 | 0.23 | 0.07 | 0.06 | 0.09 | 1.43 | 2.6 | 0.43 | 7.84 | 1.64 | 0.71 |
| 29.8 | 2190 | 260 | 2.60 | 3.49 | 3.42 | 0.07 | 0.08 | 0.09 | 0.22 | 0.13 | 0.08 | 0.07 | 0.09 | 1.42 | 2.59 | 0.45 | 7.45 | 1.54 | 0.72 |
| 32.5 | 2362 | 345 | 2.46 | 4.00 | 3.22 | 0.08 | 0.09 | 0.09 | 0.23 | 0.12 | 0.08 | 0.07 | 0.13 | 1.44 | 2.44 | 0.48 | 7.18 | 1.40 | 0.73 |
| 35.1 | 2507 | 414 | 2.02 | 3.02 | 2.63 | 0.08 | 0.09 | 0.10 | 0.23 | 0.10 | 0.08 | 0.07 | 0.15 | 1.44 | 2.32 | 0.51 | 6.77 | 1.30 | 0.72 |

TABLE III: Gradient-diffusion and similarity coefficients obtained from the optimization procedure applied to the turbulent fluxes and higher order correlations from the DNS.

| $t/t_c$ | $C_A^{(1111)}$ | $C_A^{(2222)}$ | $C_A^{(3333)}$ | $\sigma_\rho$ | $\sigma_K$ | $\sigma_\epsilon$ | $C_{pu}$ | $C_{pu}^\epsilon$ | $\sigma_m$ | $\sigma_S$ | $\sigma_\chi$ | $C_{\epsilon 0}$ | $C_{\epsilon 2}$ | $C_\chi$ | $C_{\chi 0}$ | $C_{\chi 2}$ | $C_{\chi 3}$ |
|---|---|---|---|---|---|---|---|---|---|---|---|---|---|---|---|---|---|
| 0 | 1.00 | − | 1.00 | −0.18 | 0.12 | 0.02 | − | − | −0.18 | 0.91 | 0.94 | 0.52 | 0.91 | 0.50 | 0.79 | −0.12 | − |
| 0.85 | 0.25 | −0.95 | −0.72 | 0.49 | 0.56 | 0.94 | 0.59 | 0.017 | 0.49 | 0.95 | 0.99 | 0.70 | 0.48 | 0.69 | 0.90 | −0.59 | −0.62 |
| 1.71 | −0.17 | −0.96 | −0.86 | 0.93 | 0.52 | 0.98 | 0.77 | 0.52 | 0.93 | 0.99 | 0.99 | 0.84 | 0.71 | 0.82 | 0.92 | −0.80 | −0.83 |
| 2.57 | −0.87 | −0.93 | −0.69 | 1.00 | 0.78 | 0.96 | 0.83 | 0.76 | 1.00 | 1.00 | 0.97 | 0.91 | 0.88 | 0.94 | 0.94 | −0.87 | −0.87 |
| 5.13 | −0.89 | −0.50 | 0.74 | 0.99 | 0.99 | 0.93 | 0.83 | 0.90 | 0.99 | 0.98 | 0.81 | 0.98 | 0.99 | 0.89 | 0.98 | −0.07 | −0.86 |
| 7.18 | −0.81 | −0.52 | 0.86 | 0.98 | 0.98 | 0.88 | 0.63 | 0.89 | 0.98 | 0.95 | 0.72 | 0.98 | 1.00 | 0.86 | 0.99 | 0.51 | −0.79 |
| 10.1 | 0.59 | −0.59 | 0.88 | 0.94 | 0.98 | 0.90 | 0.54 | 0.73 | 0.94 | 0.90 | 0.68 | 0.98 | 1.00 | 0.88 | 0.95 | 0.74 | 0.33 |
| 12.6 | 0.85 | 0.41 | 0.89 | 0.87 | 0.98 | 0.96 | 0.84 | 0.37 | 0.87 | 0.93 | 0.85 | 0.96 | 0.99 | 0.91 | 0.96 | 0.93 | 0.96 |
| 14.9 | 0.92 | 0.53 | 0.94 | 0.90 | 0.98 | 0.96 | 0.86 | 0.72 | 0.90 | 0.95 | 0.93 | 0.97 | 0.98 | 0.92 | 0.96 | 0.97 | 0.99 |
| 17.3 | 0.93 | 0.48 | 0.95 | 0.95 | 0.97 | 0.97 | 0.83 | 0.83 | 0.95 | 0.96 | 0.93 | 0.98 | 0.99 | 0.96 | 0.99 | 0.98 | 0.99 |
| 20.0 | 0.94 | 0.43 | 0.95 | 0.93 | 0.92 | 0.96 | 0.85 | 0.91 | 0.93 | 0.97 | 0.96 | 0.99 | 0.98 | 0.98 | 0.98 | 0.98 | 0.99 |
| 22.5 | 0.91 | 0.37 | 0.92 | 0.89 | 0.93 | 0.93 | 0.89 | 0.95 | 0.88 | 0.97 | 0.97 | 1.00 | 0.98 | 0.99 | 0.98 | 0.98 | 0.99 |
| 25.1 | 0.81 | 0.38 | 0.88 | 0.86 | 0.94 | 0.93 | 0.89 | 0.97 | 0.86 | 0.96 | 0.95 | 1.00 | 0.98 | 0.99 | 0.96 | 0.98 | 0.99 |
| 27.4 | 0.77 | 0.39 | 0.88 | 0.87 | 0.93 | 0.94 | 0.89 | 0.97 | 0.87 | 0.93 | 0.97 | 1.00 | 0.98 | 0.99 | 0.97 | 0.97 | 0.99 |
| 29.8 | 0.80 | 0.36 | 0.91 | 0.91 | 0.90 | 0.95 | 0.89 | 0.98 | 0.91 | 0.95 | 0.97 | 1.00 | 0.98 | 0.98 | 0.95 | 0.98 | 0.99 |
| 32.5 | 0.86 | 0.43 | 0.94 | 0.93 | 0.87 | 0.95 | 0.87 | 0.97 | 0.93 | 0.96 | 0.85 | 0.99 | 0.96 | 0.96 | 0.97 | 0.96 | 0.99 |
| 35.1 | 0.74 | 0.47 | 0.84 | 0.86 | 0.87 | 0.95 | 0.87 | 0.98 | 0.86 | 0.88 | 0.85 | 0.98 | 0.96 | 0.94 | 0.93 | 0.96 | 0.99 |

TABLE IV: Correlation coefficients $r$ for the generalized Boussinesq, turbulent flux, and similarity models.

| $t/t_c$ | $C_A^{(1111)}$ | $C_A^{(2222)}$ | $C_A^{(3333)}$ | $\sigma_\rho$ | $\sigma_K$ | $\sigma_\epsilon$ | $C_{pu}$ | $C_{pu}^\epsilon$ | $\sigma_m$ | $\sigma_S$ | $\sigma_\chi$ | $C_{\epsilon 0}$ | $C_{\epsilon 2}$ | $C_\chi$ | $C_{\chi 0}$ | $C_{\chi 2}$ | $C_{\chi 3}$ |
|---|---|---|---|---|---|---|---|---|---|---|---|---|---|---|---|---|---|
| 0 | 0.67 | $\infty$ | 0.67 | 0.74 | 0.07 | 0.19 | − | − | 0.74 | 0.86 | 0.93 | 0.00 | 0.91 | 0.77 | 0.83 | 0.34 | 0.00 |
| 0.85 | 0.91 | 346 | 0.73 | 0.90 | 0.41 | 0.91 | 0.46 | 0.02 | 0.90 | 0.94 | 0.98 | 0.80 | 0.71 | 0.84 | 0.93 | 0.73 | 0.13 |
| 1.71 | 1.10 | 107 | 0.79 | 0.98 | 0.45 | 0.93 | 0.54 | 0.52 | 0.98 | 0.98 | 0.97 | 0.89 | 0.87 | 0.93 | 0.93 | 0.73 | 0.18 |
| 2.57 | 1.09 | 48.9 | 0.87 | 1.00 | 0.72 | 0.89 | 0.78 | 0.76 | 1.00 | 0.99 | 0.96 | 0.94 | 0.94 | 0.97 | 0.94 | 0.76 | 0.31 |
| 5.13 | 0.96 | 17.5 | 0.97 | 1.00 | 0.96 | 0.82 | 0.82 | 0.90 | 1.00 | 0.97 | 0.80 | 0.99 | 0.99 | 0.99 | 0.98 | 0.96 | 0.62 |
| 7.18 | 1.01 | 18.1 | 0.96 | 1.00 | 0.96 | 0.78 | 0.63 | 0.88 | 1.00 | 0.94 | 0.71 | 0.99 | 1.00 | 0.99 | 0.99 | 0.97 | 0.75 |
| 10.1 | 1.10 | 16.2 | 0.95 | 0.99 | 0.97 | 0.85 | 0.54 | 0.74 | 1.00 | 0.89 | 0.69 | 1.00 | 1.00 | 0.99 | 0.99 | 0.95 | 0.90 |
| 12.6 | 1.10 | 9.14 | 0.95 | 0.98 | 0.97 | 0.97 | 0.84 | 0.33 | 0.98 | 0.91 | 0.85 | 0.99 | 1.00 | 0.99 | 0.99 | 0.96 | 0.97 |
| 14.9 | 1.03 | 3.92 | 0.97 | 0.98 | 0.98 | 0.96 | 0.86 | 0.76 | 0.98 | 0.92 | 0.92 | 0.99 | 1.00 | 0.99 | 0.99 | 0.97 | 0.98 |
| 17.3 | 1.02 | 2.05 | 0.98 | 0.99 | 0.96 | 0.98 | 0.82 | 0.82 | 0.99 | 0.95 | 0.90 | 1.00 | 1.00 | 0.99 | 0.99 | 0.98 | 0.99 |
| 20.0 | 1.02 | 1.70 | 0.98 | 0.99 | 0.91 | 0.95 | 0.86 | 0.85 | 0.99 | 0.95 | 0.96 | 1.00 | 1.00 | 1.00 | 0.99 | 0.99 | 0.99 |
| 22.5 | 1.05 | 1.80 | 0.98 | 0.98 | 0.92 | 0.90 | 0.90 | 0.89 | 0.97 | 0.96 | 0.98 | 1.00 | 1.00 | 1.00 | 0.99 | 0.99 | 0.99 |
| 25.1 | 1.10 | 1.84 | 0.96 | 0.97 | 0.93 | 0.91 | 0.90 | 1.01 | 0.98 | 0.97 | 0.95 | 1.00 | 1.00 | 1.00 | 0.99 | 0.99 | 1.00 |
| 27.4 | 1.11 | 1.68 | 0.96 | 0.98 | 0.92 | 0.92 | 0.89 | 0.98 | 0.99 | 0.96 | 0.97 | 1.00 | 1.00 | 1.00 | 0.99 | 0.99 | 1.00 |
| 29.8 | 1.10 | 1.45 | 0.96 | 0.99 | 0.90 | 0.95 | 0.88 | 1.00 | 0.99 | 0.93 | 0.97 | 1.00 | 1.00 | 1.00 | 0.99 | 0.99 | 0.99 |
| 32.5 | 1.06 | 1.24 | 0.97 | 0.99 | 0.87 | 0.96 | 0.86 | 0.93 | 0.98 | 0.95 | 0.84 | 1.00 | 0.99 | 0.99 | 0.99 | 0.98 | 0.99 |
| 35.1 | 1.18 | 1.50 | 0.92 | 0.98 | 0.88 | 0.95 | 0.85 | 1.01 | 0.98 | 0.96 | 0.84 | 1.00 | 0.99 | 0.99 | 0.99 | 0.98 | 0.99 |

TABLE V: Amplitude coefficients $a$ for the generalized Boussinesq, turbulent flux, and similarity models.

[1] O. Schilling and N. J. Mueschke, Phys. Fluids **22**, 105102 (2010).

[2] N. J. Mueschke and O. Schilling, Phys. Fluids **21**, 014106 (2009).

[3] N. J. Mueschke, M. J. Andrews, and O. Schilling, J. Fluid Mech. **567**, 27 (2006).

[4] P. A. Libby and F. A. Williams, in *Turbulent Reacting Flows*, edited by P. A. Libby and F. A. Williams, 1 (Academic Press, New York, 1994).

[5] W. P. Jones, in *Turbulent Reacting Flows*, edited by P. A. Libby and F. A. Williams, 309 (Academic Press, New York, 1994).

[6] C.-J. Chen and S.-Y. Jaw, *Fundamentals of Turbulence Modeling*, Combustion: An International Series (Taylor and Francis, 1998).

[7] P. A. Durbin and B. A. Petterson Reif, *Statistical Theory and Modeling for Turbulent Flows* (Wiley, New York, 2001).

[8] W. P. Jones and B. E. Launder, Int. J. Heat and Mass Transfer **15**, 301 (1972). Erratum, Int. J. Heat and Mass Transfer **16**, 2128 (1973).

[9] C. Chen, J. J. Riley, and P. A. McMurtry, Comb. Flame **87**, 257 (1991).

[10] D. L. Youngs, Phil. Trans. Royal Soc. London A **371**, 20120173 (2013).

[11] N. J. Mueschke, O. Schilling, D. L. Youngs, and M. J. Andrews, J. Fluid Mech. **632**, 17 (2009).

[12] P. Chassaing, R. A. Antonia, F. Anselmet, L. Joly, and S. Sarkar, *Variable Density Fluid Turbulence*, Fluid Mechanics and its Applications Vol. 69, (Kluwer Academic, Amsterdam, 2002).

[13] S. B. Pope, *Turbulent Flows* (Cambridge University Press, New York, 2000).

[14] G. Dimonte and R. Tipton, Phys. Fluids **18**, 085101 (2006).

[15] N. Peters, *Turbulent Combustion*, Cambridge Monographs on Mechanics (Cambridge University Press, New York, 2000).

[16] R. S. Cant and E. Mastorakos, *An Introduction to Turbulent Reacting Flows* (World Scientific, Singapore, 2007).

[17] A. Lipatnikov, *Fundamentals of Premixed Turbulent Combustion* (CRC Press, Boca Raton, 2013).

[18] J. W. Deardorff, J. Atmos. Sci. **23**, 503 (1966).

[19] J. W. Deardorff, J. Geophys. Res. **77**, 5900 (1972).

[20] T. Gerz and U. Schumann, Theoret. Comput. Fluid Dyn. **8**, 169 (1996).

[21] P. Chassaing, Annu. Rev. Fluid Mech. **66**, 293 (2001).

[22] F. G. Schmitt, B. Merci, E. Dick, and C. Hirsch, J. Turb. **4**, 1 (2003).

[23] F. G. Schmitt, Compt. Rendus Mecanique **335**, 617 (2007).

[24] S. Jakirlić and K. Hanjalić, J. Fluid Mech. **459**, 139 (2002).

[25] S. Parneix, D. Laurence, and P. A. Durbin, ASME J. Fluids Eng. **120**, 40 (1998).

[26] B. E. Launder and B. I. Sharma, Lett. Heat and Mass Transfer **1**, 131 (1974).

[27] B. J. Daly and F. H. Harlow, Phys. Fluids **13**, 2634 (1970).

[28] J. L. Lumley, Adv. Appl. Mech. **18**, 123 (1978).

[29] S. A. Orszag, I. Staroselsky, W. S. Flannery, and Y, Zhang, in *Simulation and Modeling of Turbulent Flows*, edited by T. B. Gatski, M. Y. Hussaini, and J. L. Lumley (Oxford University Press, Oxford, 1996).

[30] Y. Liu and R. O. Fox, AIChE J. **52**, 731 (2006).

[31] K. W. Brinkman, W. H. Calhoon, and S. M. Dash, AIAA J. **45**, 1036 (2007).

[32] P. B. Spitz and J.-F. Haas, in *Proceedings of the Third International Workshop on the Physics of Compressible Turbulent Mixing*, Royaumont, France, edited by D. Besnard, J.-F. Haas, P.-A. Holstein and B. Sitt, 511 (1991).

[33] D. M. Snider and M. J. Andrews, ASME J. Fluids Eng. **118**, 55 (1996).

[34] O. Grégoire and D. Souffland, in *Proceedings of the Seventh International Workshop on the Physics of Compressible Turbulent Mixing*, July 1999, 252.

[35] D. Besnard, F. H. Harlow, R. M. Rauenzahn, and C. Zemach, Los Alamos National Laboratory Report LA-12303-MS (1992).

[36] V. P. Chiravalle, Laser Part. Beams **24**, 381 (2006).

[37] A. Banerjee, R. A. Gore, and M. J. Andrews, Phys. Rev. E **82**, 046309 (2010).

[38] D. C. Pruett and N. A. Adams, Phys. Fluids **12**, 1133 (2000).

[39] S. Nishiki, T. Hasegawa, R. Borghi, and R. Himeno, Combust. Theory Mod. **10**, 39 (2006).

[40] S. T. Smith and R. O. Fox, Phys. Fluids **19**, 085102 (2007).

[41] A. Moreau, O. Teytaud, and J. P. Bertoglio, Phys. Fluids **18**, 105101 (2006).

[42] J. O. Hinze, *Turbulence*, second edition (McGraw-Hill, New York, 1975).

[43] G. L. Brown and A. Roshko, J. Fluid Mech. **64**, 775 (1974).

[44] N. J. Mueschke and O. Schilling, Phys. Fluids **21**, 014107 (2009).

[45] V. Adumitroaie, J. R. Ristorcelli, and D. B. Taulbee, Phys. Fluids **11**, 2696 (1999).

[46] K. Hanjalić, Annu. Rev. Fluid Mech. **34**, 321 (2002).

[47] K. Hanjalić and S. Kenjeres, in *Closure Strategies for Turbulent and Transitional Flows*, edited by B. Launder and N. Sandham, 659 (Cambridge University Press, Cambridge, 2002).

[48] K. Hanjalić and S. Kenjeres, ASME J. Fluid Eng. **73**, 430 (2006).

[49] D. Taulbee and J. VanOsdol, AIAA Paper 91-0524 (1991).

[50] S. Sarkar and B. Lakshmanan, AIAA J. **29**, 743 (1991).

[51] D. Veynante and L. Vervisch, Prog. Energy and Combust. Sci. **28**, 193 (2002).

[52] S. Gauthier and M. Bonnet, Phys. Fluids A **2**, 1685 (1990).

[53] J. T. Morán-López and O. Schilling, High Energy Density Phys. **9**, 112 (2013).

[54] J. T. Morán-López and O. Schilling, Shock Waves **24**, 325 (2014).

[55] T. Poinsot and D. Veynante, *Theoretical and Numerical Combustion*, second edition (R. T. Edwards, 2005).

[56] R. O. Fox, *Computational Models for Turbulent Reacting Flows*, Cambridge Series in Chemical Engineering (Cambridge University Press, Cambridge, 2003).

[57] S. Corrsin, J. Appl. Phys. **22**, 469 (1951).

[58] D. B. Spalding, Chem. Eng. Science **26**, 95 (1971).

[59] J. R. Ristorcelli, Phys. Fluids **18**, 075101 (2006).

[60] J. R. Ristorcelli and T. T. Clark, J. Fluid Mech. **507**, 213 (2004).

[61] N. Chidambaram, S. M. Dash, and D. C. Kenzakowski, J. Propul. Power **17**, 79 (2001).

[62] A. Mura and R. Borghi, Combust. and Flame **133**, 193 (2003).

[63] A. Mura, V. Robin, and M. Champion, Combust. Flame **149**, 217 (2007).

[64] A. Mura, K. Tsuboi, and T. Hasegawa, Combust. Theory and Mod. **12**, 671 (2008).

[65] X. Xiao, J. R. Edwards, H. A. Hassan, and A. D. Cutler, AIAA J. **44**, 593 (2006).

[66] X. Xiao, H. A. Hassan, and R. A. Baurle, AIAA J. **45**, 1415 (2007).

[67] P. Keistler, M.S. thesis, North Carolina State University (2006).

[68] W. P. Jones and P. Musonge, Phys. Fluids **31**, 3589 (1988).

[69] K. Hanjalić, S. Kenjereš, and F. Durst, Int. J. Heat and Mass Transfer **39**, 1407 (1996).

[70] S. Kenjereš and K. Hanjalić, Phys. Rev. E **62**, 7987 (2000).

[71] F. Liu and J. X. Wen, Fire Safety J. **37**, 125 (2002).

[72] W. S. Cleveland, J. Amer. Statist. Assoc. **74**, 829 (1979).

[73] W. S. Cleveland and S. J. Devlin, J. Amer. Stat. Assoc. **83**, 596 (1988).